The present work was submitted to the institute Experimentalphysik IV C (JCNS-2)

Master thesis

Efficiency of a mesitylene based cold moderator system for a compact accelerator driven neutron source

Submitted by
Mathias Strothmann
Student ID no.: 390018

1st examiner
Prof. Dr. rer. nat. habil. Thomas Brückel

2nd examiner
apl. Prof. Dr. rer. nat. Oliver Pooth

Aachen, 14.9.2020

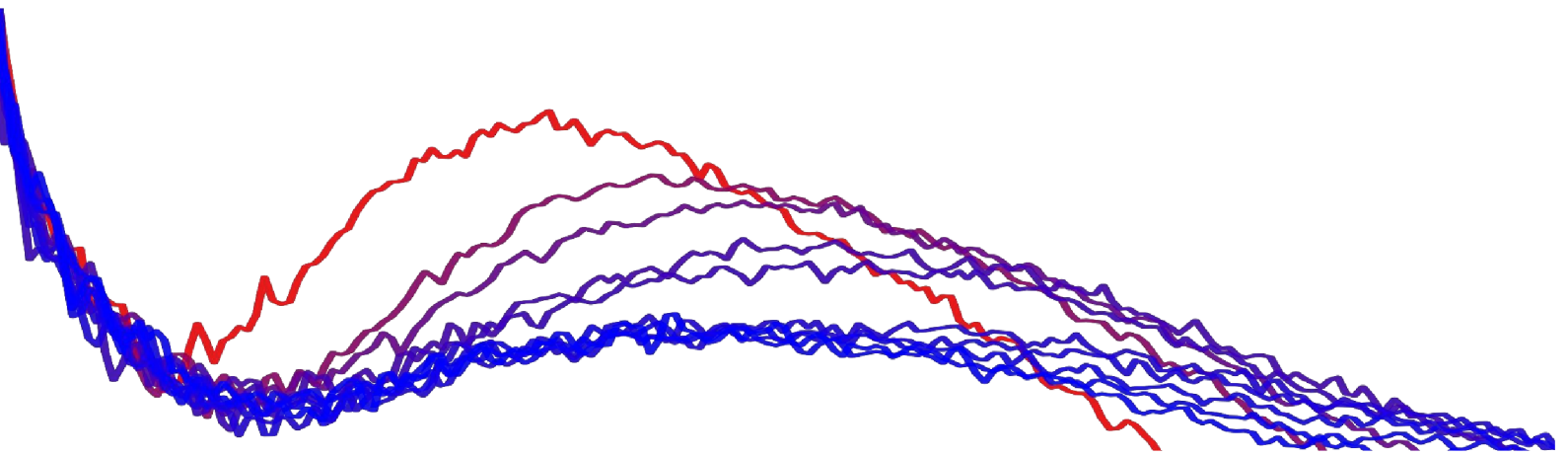

Contents

1 Introduction

In many scientific fields like nanotechnologies, energy engineering or biotechnology to give just a few examples, neutron based analytic techniques furnish powerful tools. The neutron supply is currently mainly provided by large scale facilities based on reactor and spallation sources. In Europe this landscape is changing strongly due to the decommissioning of several facilities like BER II in Germany (permanent shutdown on 11.12.2019 [13]) and ORPHEE in France (permanent shutdown 29.10.2019 [13]). On the other hand the initial start of the European Spallation Source (ESS) as a world leading project build in Lund, Sweden by an European collaboration is postponed. New large scale facilities based on spallation or reactor sources are cost intensive and also hard to realise due to political issues. Therefore a gap in the supply of the community with neutron beam days could open up, which can be encountered by new promising approaches in the development of Compact Accelerator-driven Neutron Sources (CANS). These concepts base on nuclear reactions of protons/deuterons in a suitable target material. The High Brilliance neutron Source (HBS) project aims to develop a CANS which will provide neutron fluxes at the sample position comparable to medium flux reactor sources in a scalable cost efficient facility [26]. This will be possible by the accelerator, target/moderator/shielding assembly as well as neutron optics and instrumentation optimised in every single component. In contrast to traditional reactor or spallation sources where one source/moderator serves many different instruments, the HBS project aims to produce tailored neutron beams demanded by the particular requirements of a specific measurement method. With this new promising concept of a CANS the delineate shortage of neutrons can be encountered by enabling a basic supply for neutron experiments complementary to remaining and new build large scale facilities.
The cold moderation is a crucial element in the optimisation process of the HBS project. A unique feature of the HBS is the use of low dimensional cold finger moderators. In this concept which has been patented by the Forschungszentrum Jülich GmbH [14], a so called "cold finger moderator" is inserted into an extraction channel inside a thermal moderator/reflector. Therefore the cold moderator can be placed in the maximum flux of thermal neutrons which increases the flux of useable cold neutrons significantly. An experimental validation of the low dimensional cold finger concept has been done with a liquid hydrogen based moderator system by T. Cronert et al. in 2015 [5].

Cold moderator systems can be constructed basing on different moderator materials. In this thesis the efficiency of a mesitylene based cold moderator system as component of the HBS project is investigated in an experimental setup. The measurements have been performed in the Big Karl experimental hall, which is part of the COSY facility of Forschungszentrum Jülich GmbH. The contribution to the HBS project is first the experimental validation and the production of experimental data at which the simulations can be tested, and further the gathering of specific technical experiences, regarding the engineering and handling of cold moderator systems.

The overall performance of such a moderator system is a combination of the moderator material, but is also strongly depending on the geometry. It will be shown here that mesitylene is a good choice for a system which combines a sufficient cold moderation efficiency with a robust, easy to handle and reliable technical realisation.

In chapter 2 the HBS project will be explained in more detail. After this the theoretical concept of the moderation process and mesitylene as a moderator material is shown in chapter 3. In chapter 4 the setup used for the experimental investigation of the efficiency of a mesitylene based cold moderator system is presented. Chapter 5 explains the experimental methods used in the experiment following the data preparation, analysation and interpretation of the obtained data. A conclusion of the thesis is given in chapter 7 with an outlook to improve following experiments for further investigations of mesitylene and conceptual upgrades for mesitylene based cold moderator systems.

2 The HBS project

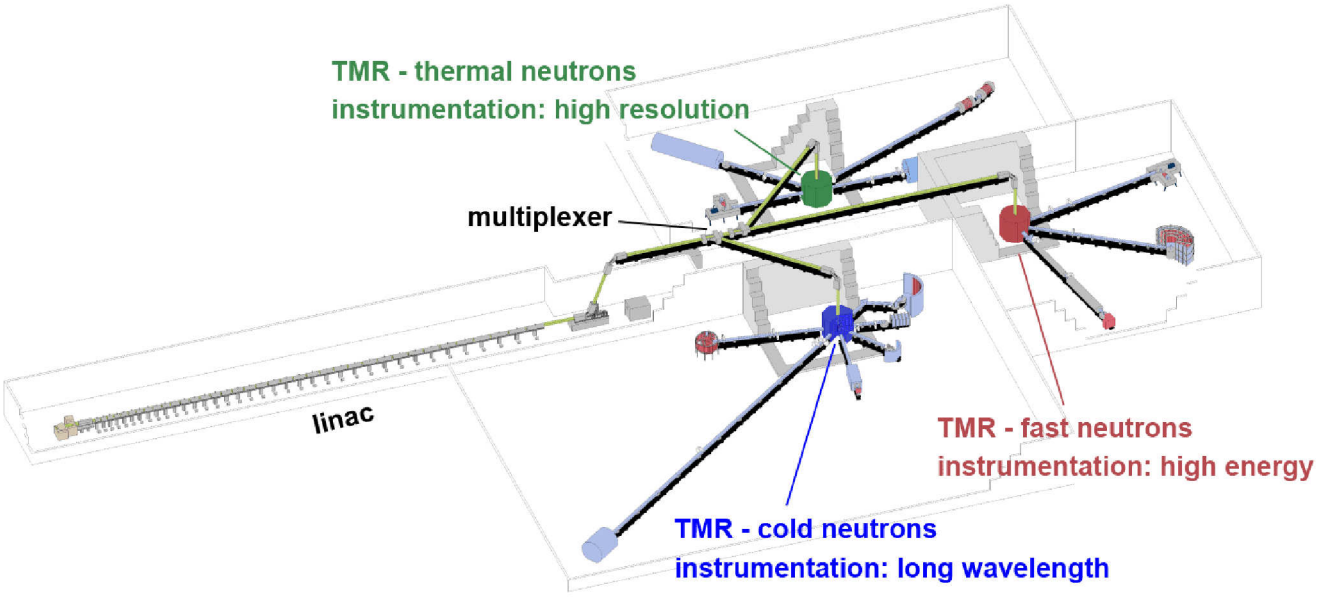

Figure 1: HBS baseline design with the central components. The linac (linear accelerator) for the production of a proton beam, the multiplexer to distribute the proton beam, the TMR (target-moderator-reflector) stations surrounded by a safety shielding and an exemplary instrumentation [11].

In this chapter an overview of the actual development state of the HBS project is presented which is based on the CDR (Conceptual Design Report) of the project [11]. The high-brilliance-source project aims at the development of a CANS concept to enable competitive fluxes at the sample position with low overall costs compared to reactor or spallation based sources. This is possible by the approach to produce the neutrons in low energy nuclear (p,n)-reactions by irradiating a target with a proton beam. Protons are accelerated by a 70 MeV linear particle accelerator (LINAC). They are distributed by a multiplexer to three different TMR (Target-Moderator-Reflector) stations. Inside the TMR the neutrons are produced by (p,n)-reactions and moderated to the desired energies by optimised thermal and cryogenic moderators. These TMR are optimised for specific instrument requirements, the pulse structure and the neutron energy. The instruments can be therefore grouped regarding their requirements and build at the same TMR.

2.1 Proton production and acceleration

The specifications for the HBS facility are heading for a proton beam of 100 mA beam current at an energy of 70 MeV capable to provide a modulated beam with pulse lengths on the µs scale with repetition rates of several hundred Hz. Additionally, a reliable operation and maintaining of the system is wanted. The technology of choice for these

requirements is a linac (linear accelerator), which is based on an ECR[1] proton source combined with a RFQ[2] based medium energy stage and a CH[3] cavity based high energy stage. The linac concept for the HBS is under development in cooperation with the Goethe-University Frankfurt.

2.2 Multiplexing

The multiplexer is designed to distribute the proton beam to the different target stations.

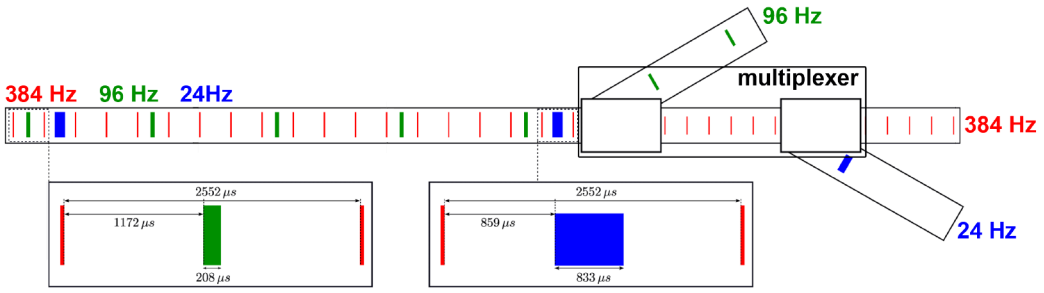

Figure 2: Illustration of multiplexed proton pulse sequence distributed to the target stations. The timings are optimised for the neutron measurement in the desired energy ranges at the different target stations (see also fig. 1) [11].

The conceptional design of the multiplexer device consists of two stages that sorts the proton pulses subsequentially. This will be provided by a combination of a fast kicker magnet to split the pulses in different beam lines followed by a septum magnet to increase the deflection angles for a further horizontal separation of the beams. Additionally, a triplet configuration of quadrupole magnets is used to refocus the beam and perform a point-to-point projection.

2.3 Target

The central component of the TMRs is the target for the neutron production in a (p,n)-reaction. The chosen target material for the HBS is tantalum. For the desired proton energy of 70 MeV it provides a high total neutron yield of $9.1 \times 10^{14}\,\mathrm{s}^{-1}\,\mathrm{mA}^{-1}$ estimated with a MCNP simulation. Ta is a material with a high strength and ductility, a high resistance against corrosion and a high melting point. Another important material property for the use as target is the high solubility of hydrogen compared to other metals. The irradiation with a proton beam causes the storage and accumulation of hydrogen in metals. This leads to blistering which reduces the withstanding of mechanical stress significantly and can lead to a damage of the target. In pure Ta, the ductility stays high even after intense proton beam irradiation. For the HBS design the target has to ensure a reliable and safe operation at a thermal power of 100 kW. Therefore a sophisticated cooling is required which will be provided by a internal water cooling through an optimised micro channel structure. Fig. 3 presents a cut through the target

[1] Electron-Cyclotron-Resonance
[2] Radio-Frequency-Quadropole
[3] Crossbar H-mode

design and shows the heat distribution and the thermal stress obtained by a FEM(finite-element-method)/CFD(computational-fluid-dynamics) simulation for a heat deposition of 100 kW.

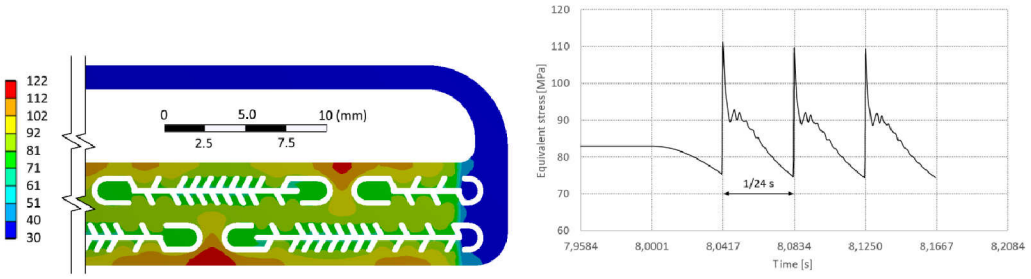

Figure 3: FEM/CFD simulation of the active water cooled multichannel target for a heat deposition of 100 kW. On the left the heat distribution in the target is shown (the color map shows temperatures in $°C$), on the right the thermal stress for a 24 Hz beam is plotted [11].

The dimensions are matched with the penetration depth of the proton beam ("Bragg peak") which is mainly dumped in the cooling water at the location of the wide channel structure behind the microchannels to prevent hydrogen accumulation inside the Ta. The color map shows a FEM ANSYS simulation of the heat distribution in the target and the induced thermal stress caused by the proton beam irradiation and gives the information that a safety operation can be achieved.

2.4 Moderation

The thermal moderator is beside the target and the neutron reflector combined to the so called TMR (Target-Moderator-Reflector) station. A cut view of the TMR is shown in fig. 4. The safety shielding of the TMR consists of an alternating layer structure of borated PE to moderate/absorb neutrons and lead to absorb the γ-radiation emitted in the neutron absorption reaction.

Due to the high hydrogen density, which provides an efficient neutron thermalisation process, high density polyethylene (PE) is the chosen material for this purpose. The thermal moderator has a diameter of 20 cm and has been investigated in a MCNP simulation shown in fig. 5. The extraction channels are placed in the maximum of the thermal neutron flux. An important advantage of the HBS concept compared to conventional reactor or spallation neutron sources arises for cold neutron demands. Every extraction channel feeding an instrument with specific demands on the neutron spectrum can be equipped with its own cold moderator which can be placed in the thermal neutron flux maximum position. For this purpose the concept of a low dimensional cold finger moderator has been developed [14].

With an optimised geometry based on the low dimensional moderator approach a trade-off between a high moderation rate and a low absorption inside the moderator material can be achieved. The tuning of these geometries in combination with different moderator materials is in progress with further simulations and experimental validation to which the results of this thesis also contributes. The two preferred moderator materials for different demands on the spectra are mesitylene, investigated in this thesis and

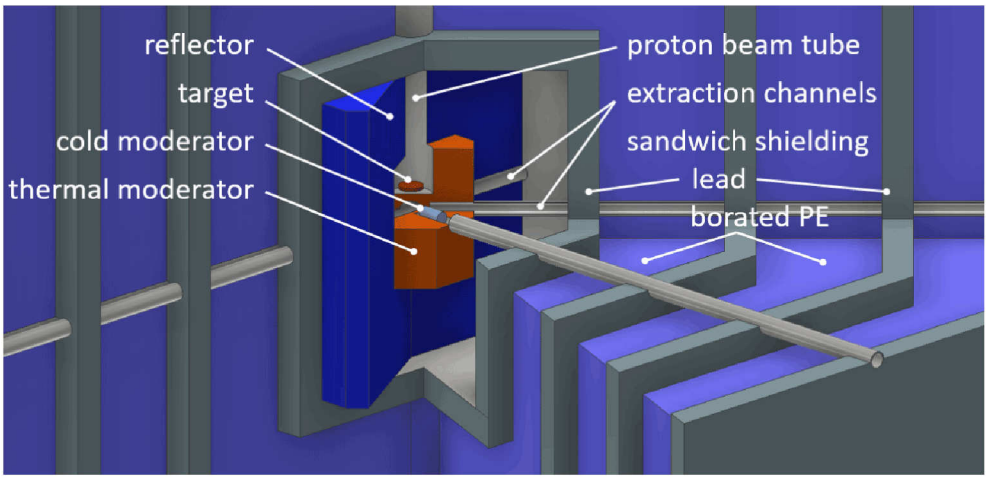

Figure 4: Inside view of a TMR with the central target irradiated from the proton beam and surrounded by the PE thermal moderator, the reflector and the sandwich structured shielding consisting of alternating layers of borated PE and lead [11].

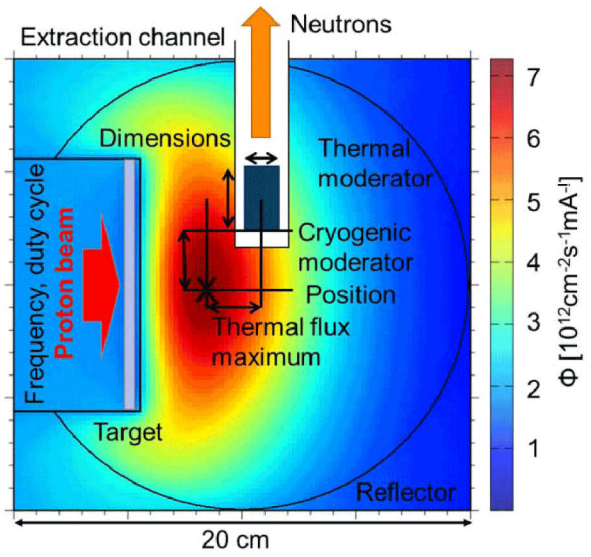

Figure 5: Thermal neutron flux (in a range between 0.4 - 2.9 Å) inside the thermal moderator surrounded by a reflector. The neutron extraction channel is placed in the maximum of the thermal neutron flux. Depending on the requested neutron spectra, a cold finger low dimensional moderator can be inserted in the extraction channel [11].

liquid H_2 with an adjustable ratio between para- and ortho-spin configuration enabling a fine tuning of the neutron spectrum.

2.5 Instrumentation

With the optimised neutron production and moderation process, a neutron flux competitive to modern reactor and low power spallation sources can be achieved for specific instrumentation. Examples for possible measurement techniques are reflectometry, SANS (small-angle-neutron-scattering), or NSE (neutron spin echo) which requires cold neutron spectra provided by the cold moderator equipped TMR with 24 Hz pulse frequency. Thermal neutron imaging and powder diffraction techniques which require higher neutron fluxes but lower energy resolution, can be placed at the TMR with 96 Hz. Here, a thermal neutrons flux (1.65 Å) up to $5.8 \cdot 10^8\, s^{-1} cm^{-2}$ will be possible. For techniques which require epithermal neutrons like PGNAA (prompt gamma neutron activation analysis) or neutron imaging, fluxes up to $5 \cdot 10^9\, s^{-1} cm^{-2}$ can be provided at the TMR operating at a 384 Hz pulse frequency.

3 Mesitylene as cold moderator

3.1 Moderation of neutrons

Neutrons and protons together form the nucleii, mediated by the four fundamental forces (weak and strong interaction, electromagnetic and gravitation force). In this thesis free neutrons are discussed, which are not bounded in nucleii and have a half-life period of 15 min until undergoing a β-decay [1]. To release neutrons from the nucleii compound, nuclear reactions between particles are needed. To gain a high neutron yield, reactions with high energetic primary particles in a MeV regime are required which leads to neutron spectra with maximum neutron energies equal to the primary particles. However, the average neutron energies of high energetic reactions are lower than the primary particle energy but still in the MeV range.

To investigate structures with neutron radiation, the corresponding wavelength of the neutrons (following from de Broglie´s law [7]) has to be comparable to the dimensions of these structures. Therefore the neutron energy has to be reduced to $=$1 eV which corresponds to a neutron wavelength of $\geq$0.3 Å. In this moderation process, the energy transfer between the neutrons and nucleii of a suitable moderator material is based mainly on an elastic kinetic momentum exchange which means that kinetic energy is transferred without a change of the energy states or the configuration of the nucleus. It has to be considered that the definition of the terms elastic/inelastic is different in the field of neutron scattering. Per collision event an amount of energy is transferred from the neutron to the moderator target atom, until the energies of the partners are equal and a state of thermal equilibrium is reached. The probability for an interaction between a neutron and a nucleus in general is given by the cross section σ of a process, which has the unit of an area surface. The larger this effective interaction surface the higher is the probability for an interaction between a neutron and a target particle.

With every interaction between the particles, also a specific probability for a neutron absorption process is associated, given by the absorption cross section σ_{abs}. The absorption cross section σ_{abs} depends on the isotope of the target nucleus and the neutron energy and is typically higher with lower neutron energies [21]. This process is inelastic due to the integration of the absorbed neutron into the target nucleus and its excitation to a higher energy state. An efficient moderator material is qualified by a high energy transfer per interaction to reduce the probability for the neutrons being absorbed in the moderation process. The maximum energy transfer proportion E_t to the target atom per collision event depends on the mass relation between the neutron mass $m_n \approx 1$ amu and the atomic number of the target atom M given by eq. 1 [10].

$$E_t = \frac{4M}{(M+1)^2} \tag{1}$$

It can be seen that the energy transfer per collision event is highest for interactions with low Z materials. Therefore hydrogen, deuterium, lithium or beryllium are preferred.

For an efficient moderator process, the needed volume of a specific moderator material is lower with a higher atomic density. Therefore the material candidates have to be solid or liquid in the desired temperature regime. For organic compound materials, a high hydrogen density is preferred.

Additionally other energy transfer processes which support the moderation capabilities arise from the lattice of solid moderators and/or the molecular structure of compounds. For neutron energies $<$4 eV (thermal and epithermal regime) a neutron

can transfer kinetic energy partial to a target molecule (respectively the lattice) by excitation of vibrational and/or rotational modes [21]. These processes are highly relevant to describe the moderation properties of organic compounds. To take the cross-sections for these energy transfers into account in simulation programs, so called $S(\alpha, \beta)$ data sets are used. The double differential cross section of collision events in compounds which transfer energy into free states given by vibrational and rotational modes can be calculated with eq.2 [21]:

$$\sigma_{E->E',\mu} = \frac{\sigma_b}{2k_B T}\sqrt{\frac{E'}{E}}S(\alpha, \beta) \tag{2}$$

With the neutron energy E before and E' after scattering, the temperature of the medium T and the bounded scattering cross section of the medium σ_b. The function $S(\alpha, \beta)$ describes the scattering law depending on the momentum transfer α (eq.3 [21]) and the energy transfer β (eq.4 [21]):

$$\alpha = \frac{E' + E - 2\mu\sqrt{E'E}}{Ak_B T} \tag{3}$$

$$\beta = \frac{E' - E}{k_B T} \tag{4}$$

In technical applications, cold neutron moderation is commonly performed in a two step process following the different requirements to the moderator material over a broad temperature range. In the first stage the high energetic neutrons are thermalised to room temperature (see also ch. 4.4). In the second stage the thermalised neutrons are moderated to cold neutron temperatures (see also ch. 4.5). In this thesis the moderation performance of mesitylene is investigated which mainly utilises the second energy transfer.

3.2 Mesitylene

Mesitylene (1,3,5-trimethylbenzene - $C_6H_3(CH_3)_3$ in the IUPAC [4] nomenclature) is an organic compound based on a benzene ring with three symmetrical attached methyl groups as depicted in fig. 6.

The substance is a colourless liquid at room temperature (boiling point at 437 K and melting point at ≈228 K [30]) with a density of $0.864\,\mathrm{g\,cm^{-3}}$ [3] and a high proton amount. Therefore it is proposed as a suitable material for cold moderator applications. Due to the symmetrically arranged, weakly hindered methyl groups bounded to a mesomeric benzene ring (depicted in fig. 6), it has rotational and vibrational degrees of freedom [30] which offer interesting benefits compared to other organic compounds in regard to the application in cold moderator systems. This is further explained in the following paragraphs. Mesitylene is safe and easy to handle. The substance is neither toxic nor carcinogenic, has a relatively high ignition point at 823 K but is still classified as being flammable [16].

[4] International Union of Pure and Applied Chemistry

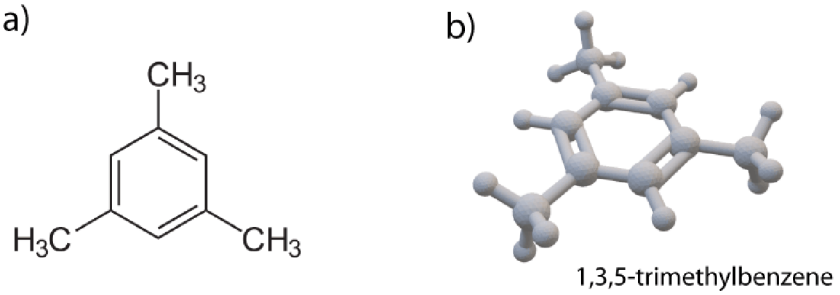

Figure 6: a) Structural formula of mesitylene [15]. b) 3D illustration of the mesitylene molecule.

Mesitylene can crystallize in three different phase states. Phase I is ordered and the only stable configuration within the whole temperature regime below its melting point at $T^{I}_{melt} = 228.4\,\mathrm{K}$ [29]. The disordered, metastable phase II has an amorphous structure (also called "protonic glass" [18]) with a melting point of $T^{II}_{melt} = 223.3\,\mathrm{K}$ [29]. Phase III is an ordered, metastable structure in a low temperature regime. The metastable phases II & III can be obtained by freezing overcooled, liquid mesitylene at slow cooling rates. Below $\approx$90 K a phase transition to phase III takes place which is reverse-able up to $\approx$180 K. A phase change from phase III (respectively phase II) can be performed by heating those phases to a range from 190 K to 220 K to start an annealing process in which a transformation to phase I occurs with a higher nucleation rate for higher temperatures. Phase II can also be cooled down below $\approx$90 K by a stabilisation of the phase state mediated by the presence of phase I nucleations [18]. Fig. 7 shows the amplitude weighted vibrational density of states $G(\nu)$ (DOS) at 20 K measured at the inverse geometry spectrometer NERA-PR at the IBR-2 reactor in Dubna by Natkaniec et al. [18]. The red marked area in the phase II spectra points out the smeared-out bands in a low energy regime which corresponds to the librations of the methyl groups in the amorphous state (the so called "boson peak"). This higher DOS for low energy compared to the ordered phases enhances the moderation efficiency especially for phase II mesitylene by giving additional states the neutron energy can be transferred into.
The moderator performance of mesitylene in phase III in comparison with ice, methane ice, and liquid hydrogen at 20 K shown in fig. 8 has been measured in the context of the JESSICA (Juelich Experimental Spallation Target Set-up In COSY Area) experiment by K. Nünighoff et al. [19] in which a target-moderator-reflector reference design for the ESS project has been investigated [21]. The spectrum of mesitylene is similar to liquid hydrogen [22], whereby mesitylene is superior in a range from 20 meV to 1 eV, corresponding to wavelengths between 2.0 Å and 0.3 Å. The performance of solid methane is distinctly higher compared to mesitylene in an energy range of 20 meV and 0.7 meV corresponding to wavelengths between 2.0 Å and 10.8 Å, but is accompanied by different disadvantages in handling, safety and duration.

The lifetime of organic compound moderators which are exposed to high radiation fields is in general limited. After irradiation, methane (and similar alkane compounds) releases hydrogen and methyl radicals. Those radicals reacts mainly in two mechanisms: (i) in an exothermal reaction two hydrogen radicals form hydrogen gas H_2 by releasing 104 kcal energy or (ii) hydrogen/methyl radicals react with each other or respectively the

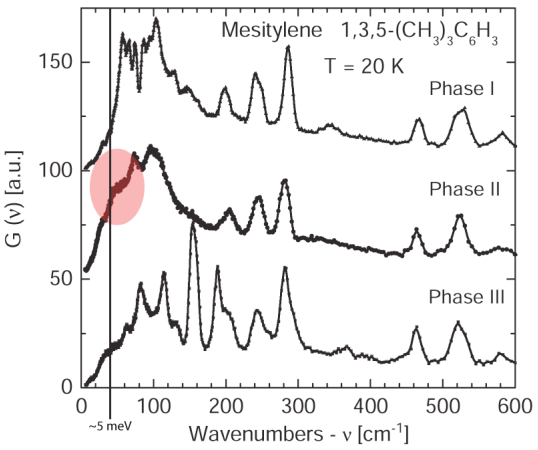

Figure 7: Vibrational spectra of different solid phases of mesitylene at $T = 20\,\mathrm{K}$ [18].

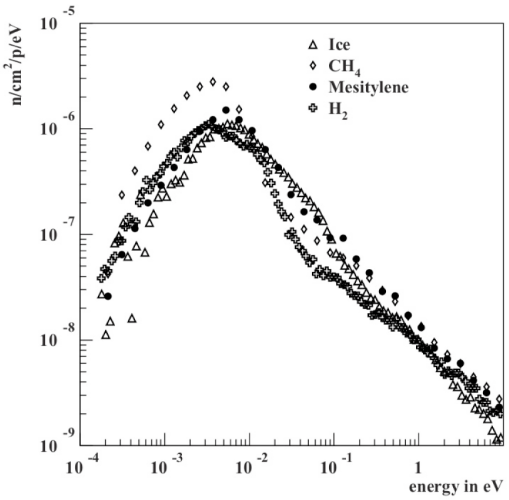

Figure 8: Neutron spectra for ice, solid methane, mesitylene (phase III) and liquid hydrogen measured at 20 K in the JESSICA experiment [19].

organic moderator compound and recombine to wax-like alkanes which can polymerise in $(\text{-CH}_2\text{-})_n$ chains. The energy released in (i) accumulates and can release spontaneously (the so called "burp") which can cause damage to the moderator container [12]. This can be avoided by an regularly annealing of the moderator. The deposits formed in (ii) reduce the efficiency of the moderator [10]. Mesitylene is less affected by radiation due to its freely rotating methyl groups and shows no spontaneous energy release [22].
In conclusion mesitylene is a high promising material for the application in cold moderator systems. The moderator efficiency is satisfying and could be increased by a crystallisation in phase II. The technical realisation of an easy to handle, affordable mesitylene based moderator system with less maintenance over a long duration period compared to alternatives like liquid hydrogen or solid methane is reasonable.

4 Measurement setup

4.1 Overview

For the presented experiments, the Big Karl experimental hall of the COSY facility in Forschungszentrum Jülich GmbH has been used.

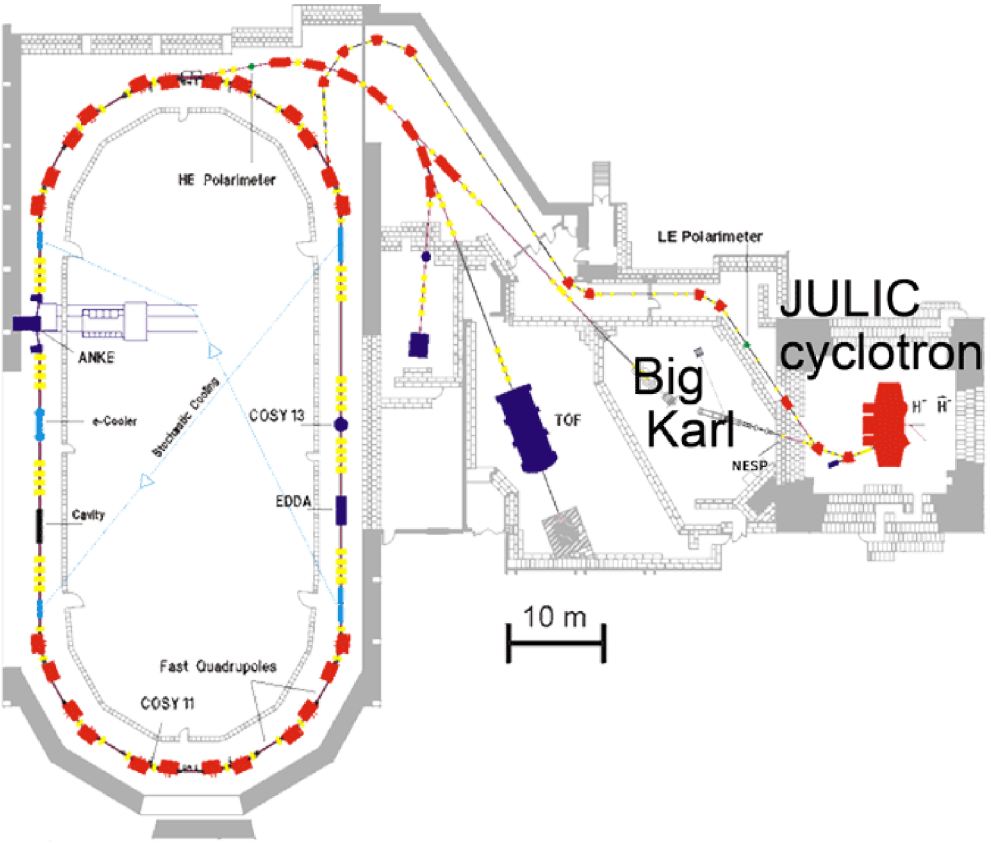

Figure 9: Site map of the COSY facility with the cooler synchrotron storage ring on the left site and the JULIC cyclotron accelerator with the neighbouring Big Karl experimental hall on the right site (true to scale). [2]

The experimental setup will be shown including (i) the acceleration of protons (ii) the neutron production in the target, (iii) the thermal moderation of the neutrons, (iv) the cold moderation, and (v) the neutron detection and measurement of the neutron spectra.

The NiederEnergiebeStrahlungsPlatz (NESP) beamline, which is fed by the cyclotron JULIC (Juelich Light Ion Cyclotron) with protons or deuterons, offers the possibility to access protons and deuterons ranging from 10 to 45 MeV and 10 to 76 MeV respectively. The maximum beam current is 10 nA in DC operation. The limitation of the current is not given by technical reasons but due to regulations of the nuclear safety in the experimental hall. It is planned in near future to increase the maximum beam current to 10 µA by enhancing the radiation shielding of the hall and the beamlines. This will further improve the capabilities of the NESP beamline for upcoming HBS experiments.

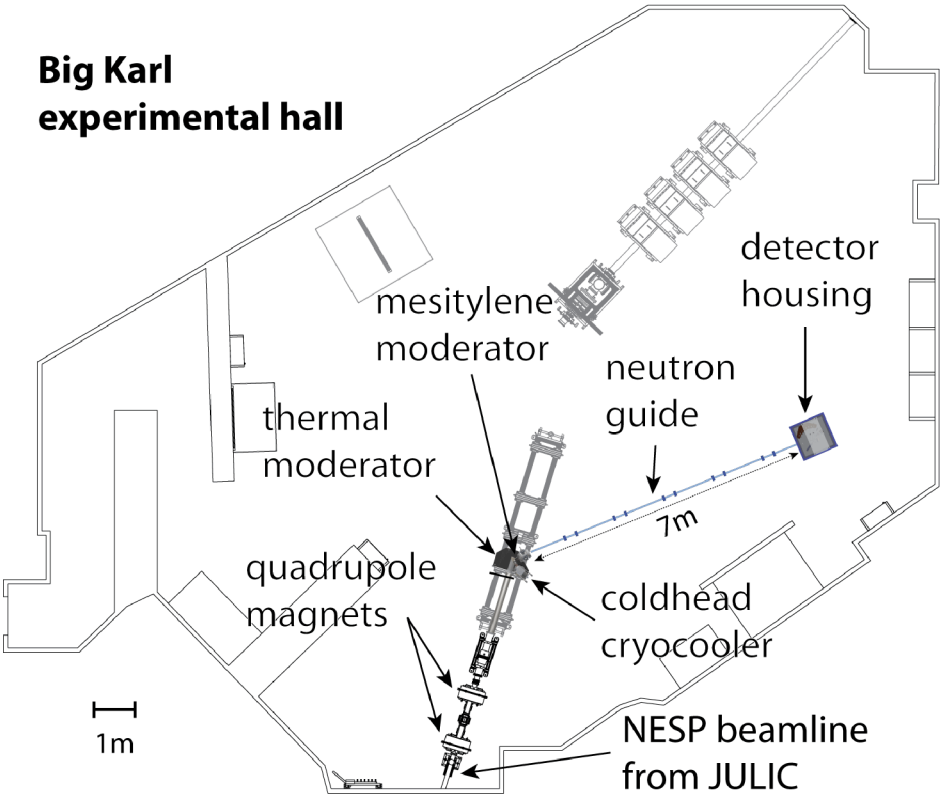

Figure 10: Big Karl experimental hall with assembled mesitylene moderator experiment setup (true to scale).

4.2 The Juelich Light Ion Cyclotron (JULIC)

The MeV proton beam that is used during the presented experiments is provided by the JULIC cyclotron accelerator. This accelerator is mainly used as injector of the COoler SYnchrotron (COSY). Alternatively, the beam guidance of the injection beamline towards COSY allows to branch off the proton/deuteron beam into the NESP beamline of the Big Karl experimental hall shown in fig. 9.

The JULIC offers H^- ions with energies up to 45 MeV and D^- ions up to 76 MeV [23]. The JULIC facility is presented in fig. 11. H^- and D^- ions are produced by a multi cusp filament volume source which provides a low energy beam of 4.5 keV and 7.6 keV, respectively, with a maximum current of 350 µA. Injecting 150 µA beam intensity into JULIC allows to extract 10 µA. Prior to injection, the ion beam passes a pulsed chopper. This so called micro-pulsing imprints a pulse structure on the beam with pulse lengths t_{pulse} with a repetition frequency f_{pulse} and a corresponding time period T_{mic}. For the experiment presented in this thesis, timings of $t_{pulse} = 200$ µs and $t_{pulse} = 500$ µs with T_{mic} of 30.3 ms, 50 ms and 80 ms were used. For the extraction of the ion beam from JULIC, an electrostatic septum is used. In order to avoid voltage breakdown from continous operation of the septum, a periodic discharge of the septum is performed. Therefore the beam is interrupted periodically every 2 s for 20 ms. This so-called macro

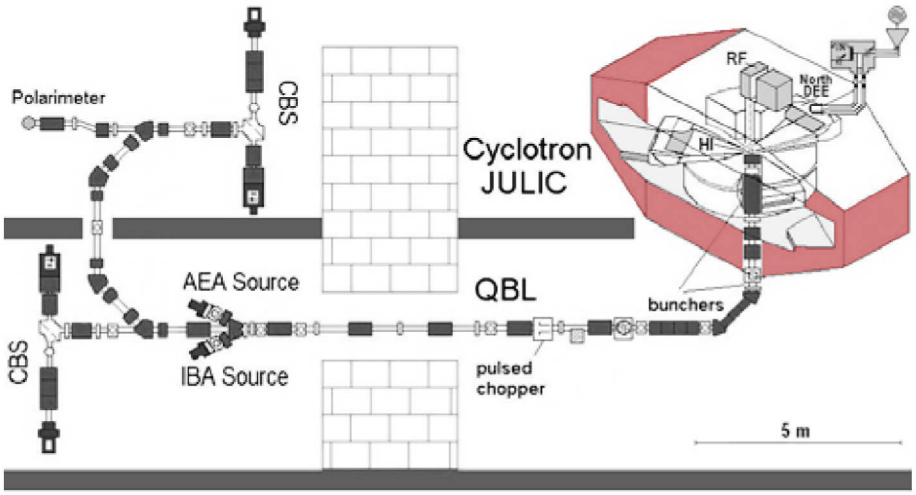

Figure 11: Sketch of the JULIC cyclotron accelerator fed by different ion sources [23].

pulsing causes an overlay of the pulse structure with a period T_{mac}. The consideration of the macro pulsing is relevant for the spectra data preparation explained in ch. 4.6.4.

The proton beam is transported through by the NESP beamline into the Big Karl experimental hall. A quadrupole magnet configuration is used to focus the beam on the target in order to reduce background. The proton beam profile of a 45 MeV proton beam shown in fig. 12 has been measured with a MWPC (Multi Wire Proportional Chamber) in the NESP beamline at a position between the quadrupole magnets and the thermal moderator assembly. It can be seen that the beam intensity projected onto the horizontal / vertical plane has a gaussian shaped profile with a maximum diameter of ≈40 mm and a FWHM of ≈20 mm. It can be assumed that the measured profile is approximately equal to the beam profile projected on the target.

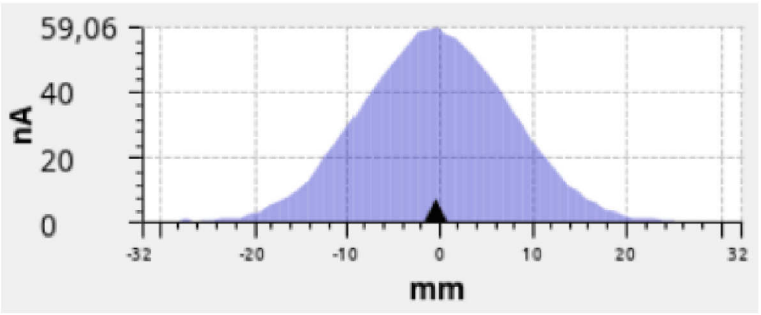

Figure 12: 45 MeV proton beam profile measured with a MWPC.

4.3 Target

A Ta target is used to produce neutrons via the (p,n)-reaction channel. This target is mounted in the target assembly which is flange mounted to the evacuated beam pipe of the proton beam line. The beam pipe vacuum includes therefore also the target assembly which is shown in detail in fig. 13. It consists of a stereolithographic (SLS) 3D printed target holder, which is vacuum seal glued to an aluminium CF vacuum flask. The material of the printed part is a UV hardened polymer resin, which has similar thermal moderation properties compared to PE. In this part the target is mounted in an angle of 45° aligned to arrange the experimental setup in the Big Karl experimental hall (see also fig. 10). The target is a Tantalum disk with a diameter of 50 mm and a thickness of 5 mm. The material and dimension of the target has been chosen regarding to the investigations in previous HBS measurements attuned to an optimised neutron yield [24].

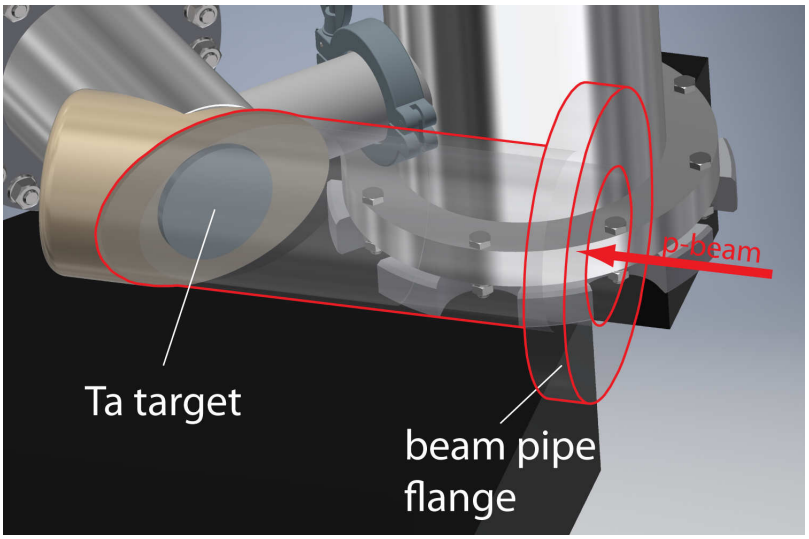

Figure 13: Rendering of the vacuum flange (transparent drawn, red wireframed) with the mounted Ta disc target, onto a 3D printed target holder.

4.4 Thermal moderator assembly

The thermal moderator sketched in fig. 14 shows the thermal moderator block made of high density polyethylene (PE) which is used to moderate the high energy neutrons to thermal energies. This organic polymer compound $(C_2H_4)_n$ has sufficient thermal moderation properties due to the high amount of hydrogen (see also ch. 3). For the inside view, the two upper segments are shown half transparent. The two inner segments are carved in the shape of the inside placed assemblies to encase these components as tight as possible to optimise the moderation efficiency and give the components static support. An extraction channel is placed at an angle of 45° extracting the neutrons from the thermal maximum.

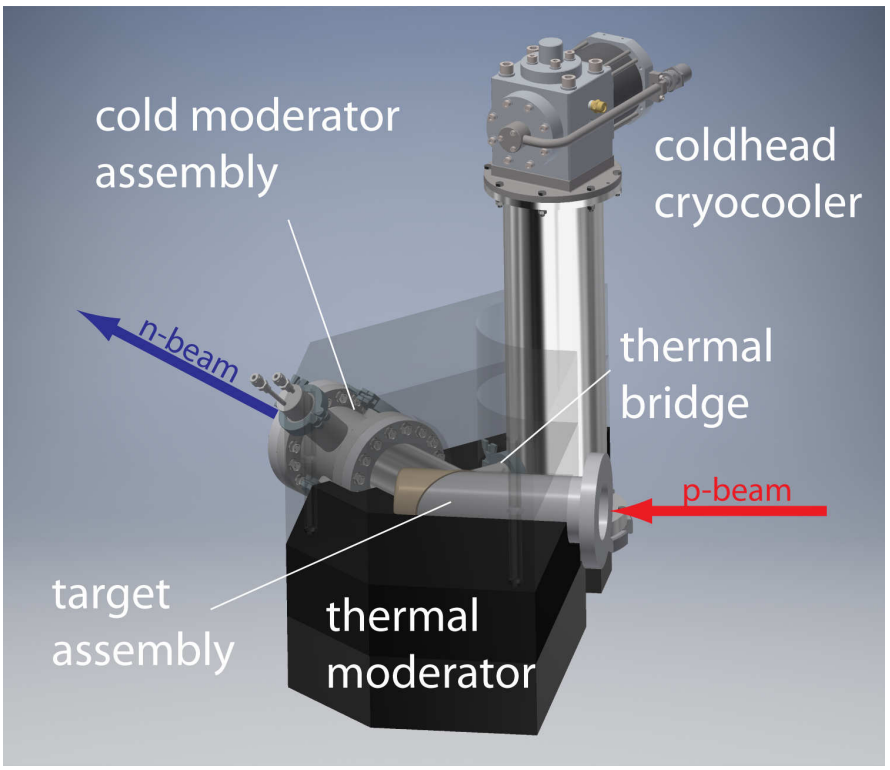

Figure 14: Rendering of the thermal moderator assembly.

4.5 Cold mesitylene moderator

A cold mesitylene moderator is placed into the extraction channel and in front of the target. The moderated neutrons are measured with the TOF setup explained in ch. 4.6. The core component of the experiment is the cold moderator assembly consisting of the mesitylene vessel attached via a conducting thermal bridge to a coldhead cryocooler device as shown in fig. 15. The housing of the assembly (shown half transparent) is impinged by an insulation vacuum of 10^{-6} mbar provided by a turbo-molecular pumping station[5] connected to a DN KF40 flange at the crosshead. The crosshead is a DN CF100 pipe element with four diametrical arranged DN KF40 flanges. At these flanges the vacuum feed-throughs for the mesitylene in- and outlet and the sensor/heater connectors are mounted.

[5]Pfeiffer Vacuum HiCube Eco 80.

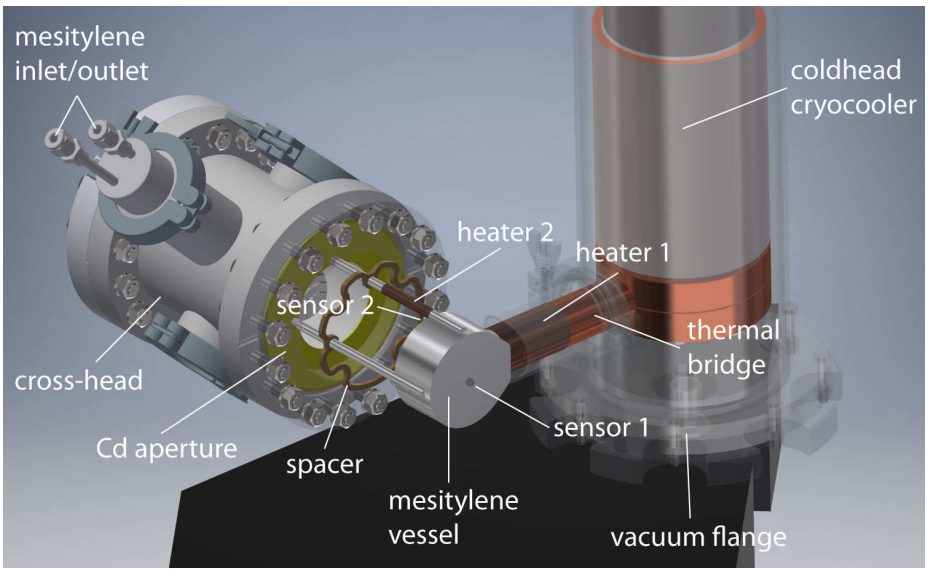

Figure 15: Rendering of the cold moderator assembly.

The moderator vessel made of aluminium has an inner dimension of 60 mm diameter and a height of 30 mm. The moderating mesitylene volume is therefore 78.5 cm^3. Components which are located in the neutron beam are mainly made of aluminium, which has a small neutron scattering and absorption cross section over a broad energy range [17] and is therefore nearly transparent to neutron radiation. The mesitylene vessel is connected with the inlet/outlet via stainless steel tubes to a vacuum feed through mounted in a DN KF40 flange of the crosshead. With these connections, a closed loop system with a mesitylene reservoir and a pump is established during the freezing process, which is described in ch. 5. A Vespel® spacer holds the tubes and the mesitylene vessel in a free standing position to prevent contact and therefore unwanted heat exchange to the assembly housing mounted to a DN CF100 flange of the crosshead. The cooling of the vessel is provided by a coldhead cryocooler thermally connected to the side of the vessel (see fig. 15) via a thermal bridge. The thermal bridge is made of copper with a diameter of 50 mm and a length of 108 mm. It is screwed into the flank of the mesitylene vessel by a threaded rod with an interlayer of indium in between. Indium has a high ductility also at cryo temperatures. Therefore it is needed as a gasket to ensure a prober thermal coupling of the parts. The opposite side of the thermal bridge is clamped connected with an indium interlayer to the coldhead device. The thermal bridge is wrapped by a heating wire and covered by Stycast® to enhance the thermal conduction between sensor, heating wire and thermal bridge. To measure the temperature of the mesitylene, a sensor diode[6] is attached to the bottom of the vessel (sensor 1). The outlet of the mesitylene vessel is wraped by a heating wire to prevent freezing of the inlet (see also ch. 5) and equipped with a temperature sensor diode[6] (sensor 2). A cadmium aperture is mounted in the crosshead (yellow marked in fig. 15) to define the neutron radiating surface of the moderator vessel coupled into the neutron guide (see ch. 4.6) and lower the neutronic background. In fig. 16 an overview of the temperature control of the moderator system and the mesitylene circle is sketched. The temperature

[6] DT601

control of the system is realised by two PID (proportional-integral-derivation) circuits of a temperature controller[7] which are connected to the sensors and heaters.

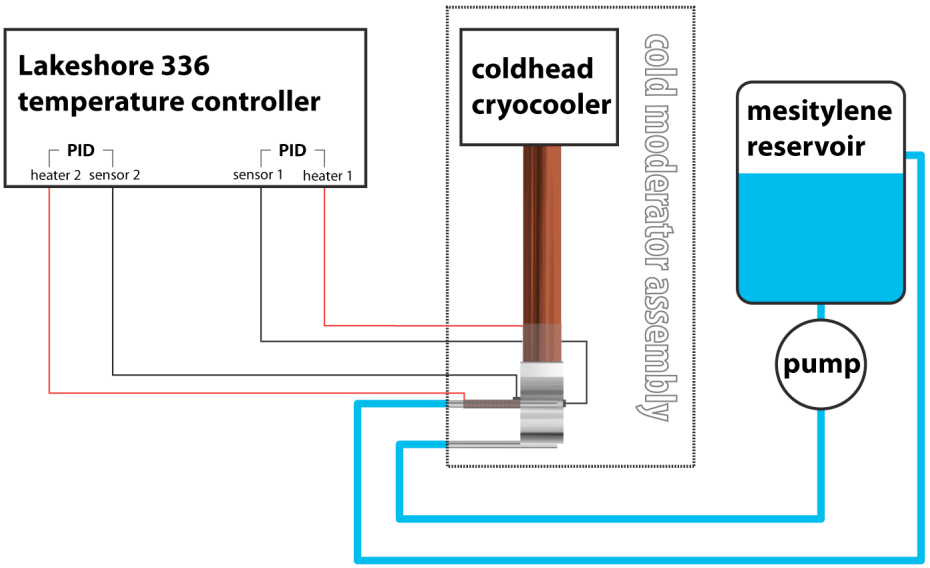

Figure 16: Sketched overview of the temperature control and closed loop mesitylene circle of the moderator system.

4.6 Detector system

The detector setup can be divided into three main components - (i) the neutron guide, (ii) the ^{3}He tube detectors and (iii) the B-PE shielding, which are sketched in fig. 17. The neutron guide is placed in front of the cold moderator assembly in the center of the neutron beam as shown in fig. 14.

[7] Lakeshore 336

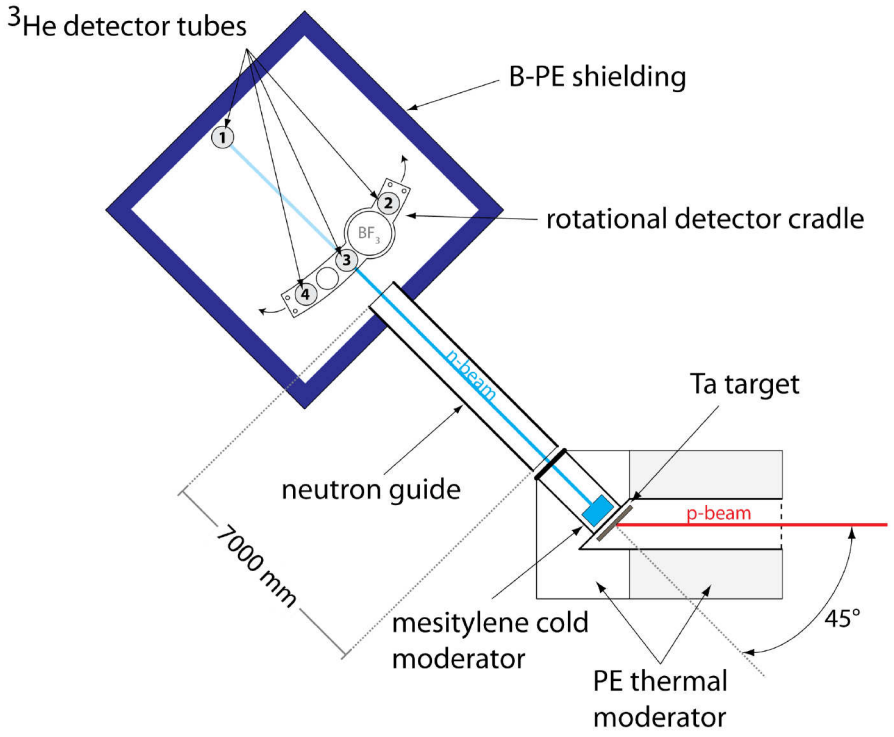

Figure 17: Overview of the neutron detector setup arranged to the moderator assemblies.

4.6.1 Neutron guide

The neutron guide leads neutrons to the detection system over a path of $l_{ng} = 7000\,\text{mm}$, needed for the TOF (Time-Of-Flight) measurement method. Such a neutron guide reduces losses in the neutron flux while it increases the gain for cold neutrons wavelength (see also ch. 6.1.3). It is positioned in front of the cold moderator assembly in the center of the neutron beam optical axis shown in fig. 18. The distance from the cap of the cold moderator vacuum chamber to the entrance of the neutron guide is 54 mm. The aluminium cap is covered by an aperture of cadmium in the size of 61 mm x 39 mm. The size of the in- and out-windows are equal to the inner dimensions of the guide with a height of 45 mm, a width of 30 mm. The neutron guide is made of glass coated by ^{58}Ni, which results in a refractive index of $m = 1.2$. To reduce neutron absorption and scattering in air, the guide is evacuated to 10^{-3} mbar. The neutron guide leads the neutron beam into the shielded detector housing shown on fig. 22.

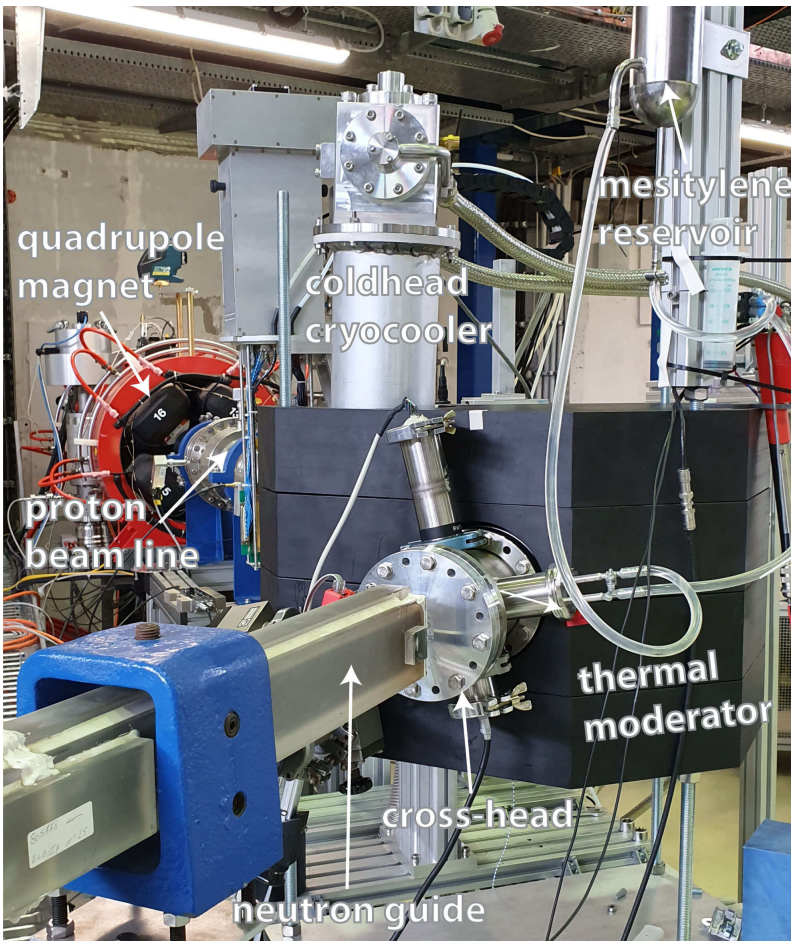

Figure 18: Neutron guide placed in front of the cold moderator and target assembly which is flanged to the proton beamline with attached quadrupole magnet. On the right upper side of the picture the closed loop mesitylene system is visible (sketched in fig. 16).

4.6.2 ^{3}He-tube detector

For the neutron measurements which are presented in ch. 6, ^{3}He-tube detectors have been used. The working principle of these proportional counter tubes is a gas discharge process. The ^{3}He isotope has a high neutron absorption cross section for a broad range of neutron energies shown in fig. 19 together with a low atomic number $Z = 2$. These properties lead to a high neutron sensitivity combined with a low γ-sensitivity of the detector system [9]. The neutron capture reaction is given in eq. 5 [9].

$$^3He + {}^1_0n \rightarrow {}^3H + {}^0_1p + 0.764\ MeV \tag{5}$$

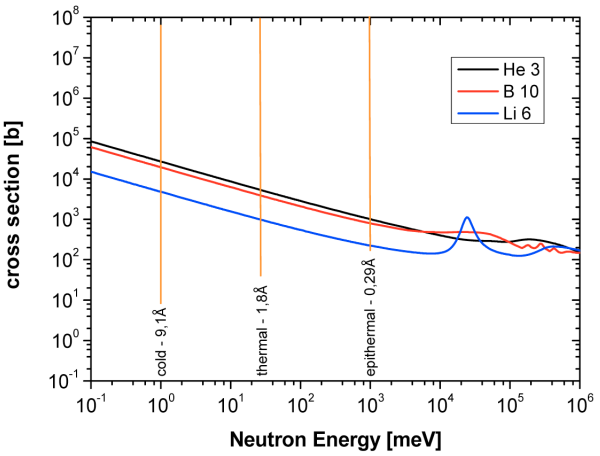

Figure 19: Absorption cross sections σ_{abs} for ^{3}He, ^{10}B and ^{6}Li in neutron capture reactions plotted against the kinetic neutron energies. [9]

In fig. 20 the working principle of a ^{3}He detector tube is displayed as cross-sectional image. Additionally, the peripheral devices for the TOF measurement are shown. The detector tubes used for the measurements have an outer diameter of 25.4 mm (1") and a length of 200 mm. The tube is made of stainless steel with a wall size of 0.8 mm and is filled with ^{3}He as active detector gas.

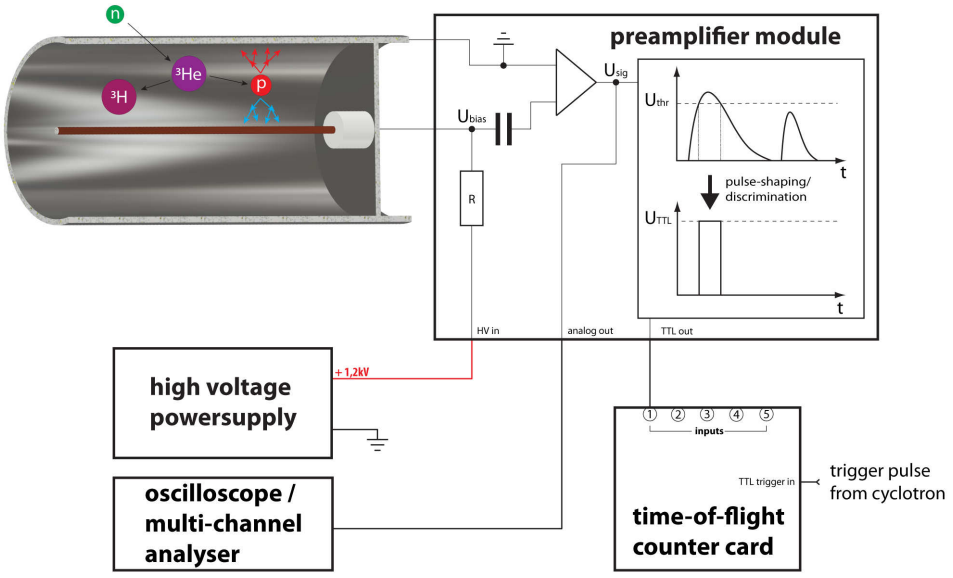

Figure 20: ^{3}He detector tube with connected peripherals for measurements in TOF mode.

In the center of the tube a wire is mounted isolated to the housing and biased with a voltage $U_{bias} = 1.2\ kV$. This causes a radial electric field gradient inside the ^{3}He filled

tube. Following eq. 5, a neutron reacts with a ^{3}He atom to a positive charged proton (depicted in red), which is accelerated by the electric field gradient caused by the bias voltage U_{bias}. It has to be considered that the energy of the proton is given by the mechanism of the capture reaction and is independent from the energy of the captured neutron. Due to the acceleration of the proton, a cascade of collisions with gas atoms takes place and releases negative charged particles (depicted in blue) by ionisation of the gas atoms. The negative charged particles (mainly electrons) are accelerated in the opposite direction in the electric field which causes likewise collision ionisations. The avalanche-like amplification of the initial α-particle leads to a cloud of charged particles. When this charge reaches the wire, it drains off and is amplified in the preamplifier module. The preamplifier module also includes circuitry for the shaping of the amplified signal pulse and the discrimination of the signal. The amplified signal pulse U_{sig} can be monitored by an oscilloscope or MCA (Multi-Channel-Analyser) at the analog output. The amplitude of the signal pulse U_{sig} depends on the applied U_{bias}, but also on the gas pressure p in the detector tube (p is evaluated further in ch. 5.4) which determines the density of gas particles available for collision ionisations. The discrimination of the signal as depicted in fig. 20 suppresses pulses which are lower then the predefined threshold voltage U_{thr}. Therefore lower energetic ionisation events mainly resulting from γ background and not related to a neutron capture reaction will be suppressed. Fig. 21 shows an exemplary energy spectra of a ^{3}He detector measured with a MCA. The pulses are binned regarding their amplitudes U_{sig} which are proportional to the energies of detected events. The red marked area shows the optimal setting of the threshold level U_{thr} next to the characteristic "triton peak" of the ^{3}He neutron capture reaction. Events caused mainly by γ-absorption have a low energy therefore U_{sig} is below U_{thr} and the event is discriminated (red marked area).

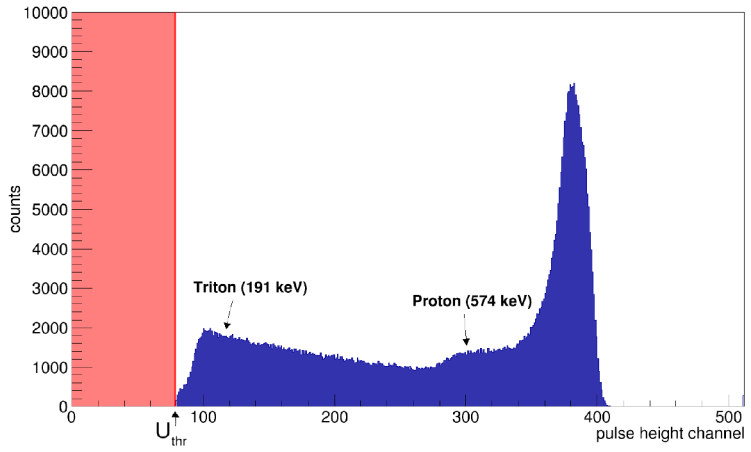

Figure 21: Exemplary energy spectra of ^{3}He detector tube recorded with a MCA. The measured pulses are binned regarding their amplitude U_{sig}. [9]

The discriminated pulse is contacted to the output of the preamplifier module in transistor-transistor-logic (TTL) standard and correlates to one detected neutron per TTL pulse. To obtain this optimal relation of one TTL pulse per neutron the sensitivity of the detection system has to be adjusted by the threshold level of the discrimination

for a suitable, constant bias voltage U_{bias} to suppress counts triggered by other initial ionisation processes than a neutron capture event.

4.6.3 Detector housing/shielding

The ^{3}He tube detectors are mounted on a rotatable cradle. The detector arrangement is shielded by borated polyethylene (B-PE) against neutronic background. An view on the detector assembly placed inside the shielding is given in fig. 22.

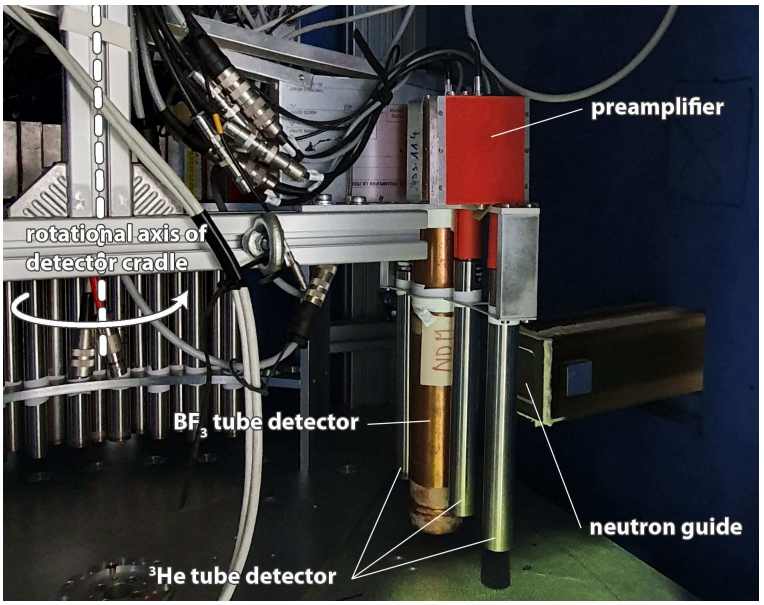

Figure 22: Inside view of the detector housing. The exit window of the neutron guide pierces through the blue coloured B-PE shielding board and is aligned to the neutron tube detectors mounted in a rotational detector cradle.

$$\begin{aligned} {}^{10}B + {}^{1}_{0}n \rightarrow \quad & {}^{7}Li + \alpha + 2,792\ MeV(6\%) \\ \rightarrow \quad & {}^{7}Li^{*} + \alpha + 2,310\ MeV(94\%) \\ & {}^{7}Li + \gamma(0.48\ MeV) \end{aligned} \tag{6}$$

The shielding of the housing consists of 40 mm thick boards of 20 % borated high density polyethylene (B-PE). This compound material has superior neutron shielding capabilities. The PE matrix thermalises fast neutrons as described in ch. 4.4. The thermalised neutrons are captured in a (n,γ)-reaction given in eq. 6 [9] due to the high absorption cross section of the added ^{10}B (see also fig. 19).

4.6.4 TOF (Time-Of-Flight) technique

The Time-Of-Flight (TOF) technique has been used to measure the neutron spectra presented in ch. 6. The basic principle is, that a neutron with a certain kinetic energy and corresponding velocity needs a defined time to reach the detector over the known

length of a flight path l_{tof}. The start for the TOF path is defined in the position of the mesitylene moderator surface. The path length is therefore the sum of the distance from the moderator surface to the neutron guide entry, the neutron guide length l_{ng} and the distance from the neutron guide exit to the front detector position which results to l_{tof} =7555 mm. The length of the neutron guide l_{ng} shown in ch. 4.6.1. To measure a neutron energy spectra, a starting time of the neutron source has to be defined. For continuous sources like reactors, this can be achieved by a chopper system which is used to modulate the beam in a defined frequency. An advantage of CANS (and also spallation sources) is the capability to modulate a pulsed neutron beam without additional hardware directly in the neutron production process by the application of a pulsed proton beam (see also ch. 4.2).

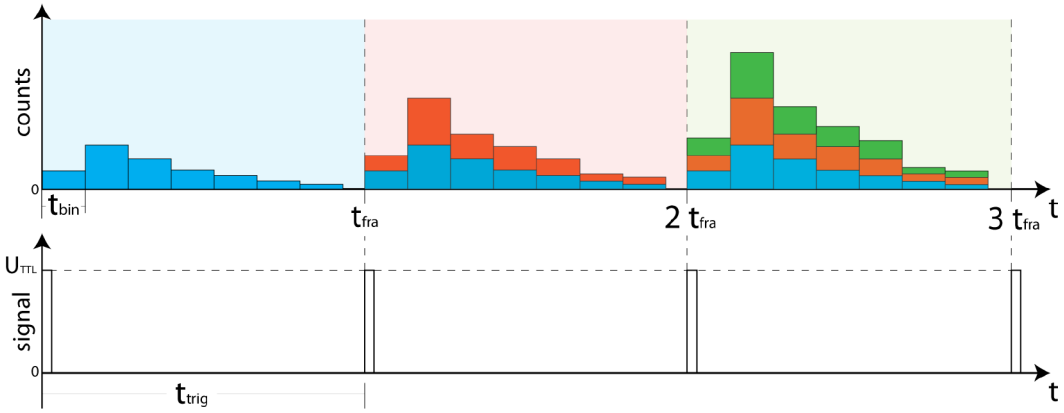

Figure 23: Diagram of TOF technique working principle. The upper plot shows the counts summed up with every following time frame. The down plot sketches the trigger signal resetting the time frame.

The start time of the neutron pulse is indicated by a trigger signal provided by the cyclotron, which is connected to the TOF counter device (sketched in fig. 20). The trigger opens a time frame for the detector input. The length t_{fra} of the frame is chosen regarding the energy range, whereby the minimal energy to be measured is given by $E_{min}[eV] = \frac{1}{2 \cdot e} \cdot m_n \cdot (\frac{l_{tof}}{t_{fra}})^2$ with the elementary charge e, mass of the neutron m_n and the length of the flight path l_{tof}. The time frame is divided into bins of t_{bin}. The TOF counter card sorts counted pulses at the input into bins regarding to the time stamp of the arrival of the neutron at the detector. Usually t_{bin} is much larger then the time interval between neutron arrival and receive of the TTL pulse in the counter card, which enfolds the neutron reaction time in the ^{3}He-tube and the processing time in the preamplifier module. Therefore it can be assumed that the count of the neutron is instantaneous with the arrival at the detector. With every trigger pulse, the next time frame is opened and summed up with the previous ones by sorting the counts in the corresponding time bins. Therefore the statistics of the distribution enhances with the amount of summed up time frames. The statistic uncertainty σ for the total number of counts n, reduces with the sum of time windows and is given by $\sigma = \sqrt{n}$.

5 Experimental methods

5.1 Filling the moderator vessel with mesitylene

The moderator vessel is connected to a closed loop system as shown previously in fig. 16 to pump the mesitylene from a reservoir into the moderator vessel. The outlet connection of the vessel is aligned upwards in a slightly tilted position to avoid air congregations. The filling process is finished when pure mesitylene, free of air bubbles, is visible in the transparent silicon tube of the return circuit, which takes $\approx$5 min. The pump should also be activated shortly before a freezing process is started to vent the system and ensure that the vessel is completely filled.

5.2 Freezing and temperature stabilisation of mesitylene

An essential element of the experiment is the cooling of the mesitylene moderator and stabilising its temperature at specific setpoints. As presented in fig. 15, the mesitylene vessel is thermally connected to a coldhead cryocooler device by a thermal bridge. The reason for this construction is (i) to place the coldhead outside the neutronic field and (ii) to add a heater to the thermal bridge. This heater enables the system to hold setpoints over a broad temperature range and is needed due to the limitations of the cryocooler. The cryocooler generates a constant thermal flux depending on the current temperature and cannot be modulated.

To operate the moderator system in a stable thermal equilibrium (setpoint of a desired temperature), a proportional-integral-derivative (PID) controller (depicted in fig. 16) has been used to pointedly counter heat the thermal bridge against the thermal flux of the cryocooler. The maximum heating power of the temperature controller´s[8] PID circuit is 50 W. A crucial constructional defiance is to avoid any heat transfer from the environment to the moderator system in order to reach the desired temperatures < 20 K. For this reason, the moderator is covered by an insulation vacuum of $\leq 10^{-6}$ mbar and decoupled from the vacuum recipient with a Vespel® spacer.
The thermal transfer from the active cooling-/heating- devices into the moderator system and the contribution of heat radiation is taken into account by a finite-element-method (FEM) simulation in ANSYS 18 [27].

[8] Lakeshore 336 cryo temperature controller

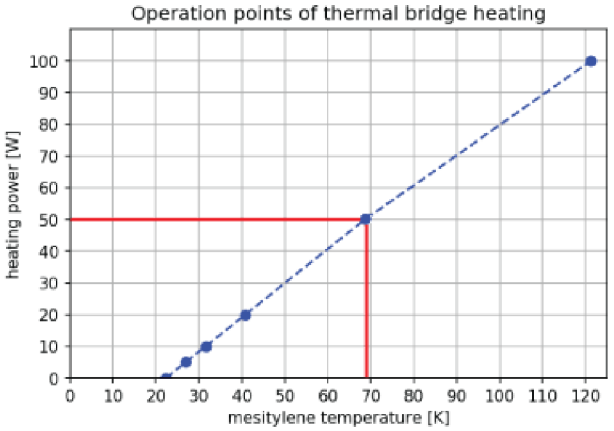

Figure 24: Diagram of temperature range of stable operation depending on thermal bridge heating power. The plotted data points are calculated with ANSYS 18 in [27]

The simulation shows that the moderator system allows stable operation in a temperature range from 20 K to 70 K for the maximum heating power of 50 W for the bridge heater[9], see fig. 24.
The heat distribution in the vessel is given by the high thermal conductivity of aluminium ($\lambda_{Al} = 230\ W \cdot m^{-1} \cdot K^{-1}$ [4]) compared to mesitylene ($\lambda_{C_9H_{12}} = 0,2\ W \cdot m^{-1} \cdot K^{-1}$ at 32 K [22]), the thermal flux maximum occurs in the vessel side, connected to the thermal bridge and is lead through the vessel walls around the mesitylene volume. Therefore the crystallisation of the mesitylene starts at the vessel walls when the melting point $T_{melt} = 227\,\mathrm{K}$ is reached and spreads radially into the liquid center. Following this consideration, the outlet freezes before the inner core is completely frozen. Pretests of shock frosting mesitylene in liquid nitrogen results in a mesitylene volume reduction of approximately 10% compared to the liquid state. To ensure an entire, homogeneous filling of the vessel in the frozen state, the outlet pipe is heated (depicted in fig. 16) near the freezing point to allow mesitylene flowing from the outlet pipe into the vessel during crystallisation.

In the beginning of the experiment, the moderator vessel has been filled and vented as described in the previous chapter. After deactivating the mesitylene pump, the cold-head cryocooler has been activated. The PID controlled counter heater 1 (thermal bridge) was set to 225 K and heater 2 (outlet heater) to 245 K to slow down the temperature decrease near the freezing point in order to allow the heat flux to distribute into the mesitylene (low thermal conductivity compared to the vessel) homogeneously. The mesitylene/moderator temperature of the experiment T_{mod} is defined as the value of sensor 1 (see also fig. 15 and fig. 16). During the cooling process, a formation of gas bubbles could be observed in the transparent tubes of the mesitylene outlet of the cold moderator assembly. This outgasing increased at a temperature $T_{mod} \sim 235\,\mathrm{K}$ while further cooling. Additionally a movement respectively slaking of the silicon tubes (see also fig. 18) could be observed. The outgasing and movement of the tubes decreased with temperatures below the freezing point of the mesitylene. Therefore it can

[9]During the experiment the also PID controlled outlet heater has been used in addition to the bridge heater, which is not taken into account in the simulation.

be assumed that highly dynamic processes take place in the moderator vessel during the cooling/crystallisation which lead to a mixing of mesitylene in different temperature states. The observed shrinking of mesitylene in the shock frost pretest was most probably given by a loss of mesitylene due to a throw-off induced by a spontaneous gas release of solved atmospheric gas due to the reduced solubility during the cooling procedure. The high amount of solved gases was confirmed by a test draw up of mesitylene inside a syringe in which as well a formation of gas bubbles was detected due to the under-pressure within the syringe.

In fig. 25 the log data of the temperature controller is shown for sensor 1 at the vessel position (see also fig. 16). Between $t = 0\,\mathrm{s}$ and $t = 1500\,\mathrm{s}$ the PID controlled counter heaters slow down the temperature decrease as described above. At $t = 1500\,\mathrm{s}$ the PID control was deactivated, therefore the coldhead runs on the maximum available power that decreases with decreasing temperature. The plateau of the minimum moderator temperature at 22 K is reached $\approx 100\,\mathrm{min}$ after the counter heater deactivation. At the minimum temperature the cooling flux of the coldhead and heat inputs of the environment which overcome the insulation are in an equilibrium. The simulation shown in fig. 24 gives a good match for the reachable minimum temperature at 22 K. The temperature range for a stable operation of the moderator system could be extended in the experiment to 180 K with a variation of 1 K. This is mainly caused by the additional counter heating using the outlet heater. After the freezing process the mesitylene has been held in the frozen state over the whole experiment. In the measurements presented in ch. 6, the temperatures has been set to 22 K, 30 K, 40 K, 52 K, 57 K, 90 K, 100 K, 140 K and 180 K.

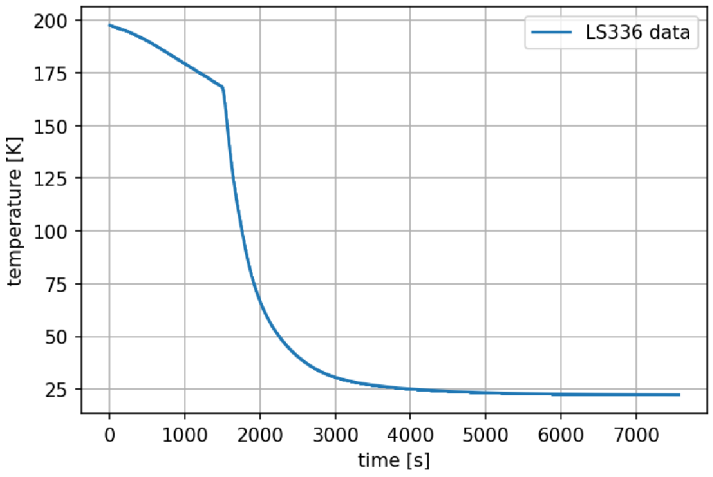

Figure 25: Diagram shows the logged data of the temperature controller at the sensor position 1 ("mesitylene vessel").

5.3 Detector alignment

In fig. 26, the detector arrangement inside the shielding is sketched. Detector 2, 3 and 4 are placed on a rotatable goniometer cradle (also shown in fig. 22) while the transmission detector 1 is fixed at the rear wall of the shielding. The cradle allows to turn the goniometer detectors in the center of the neutron beam at the neutron guide

exit which shades the transmission detector from the neutron beam (illustrated in fig. 26). The intensities of the detectors have been measured while turning them through the beam (so called "angle scan"). From these measurements the efficiency ϵ_{det} can be obtained by the difference in the intensities of the shaded and unshaded transmission detector, explained in the next chapter.

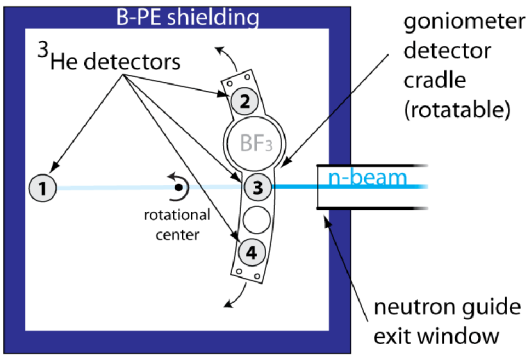

Figure 26: Illustration (not true to scale) of the detector assembly mounted inside the B-PE shielding. The light blue beam illustrates the shading of the ^{3}He transmission detector 1 by detector 3 in the front position.

5.4 Determination of ^{3}He-detector efficiency

The efficiency ϵ_{det} of the ^{3}He tube detectors is needed to correct for the characteristics of the detection system from the neutron spectra data. In the following chapter, a procedure is described to obtain this parameter from the angle scans, shown in the previous chapter. An exemplary angle scan is shown in fig. 27.

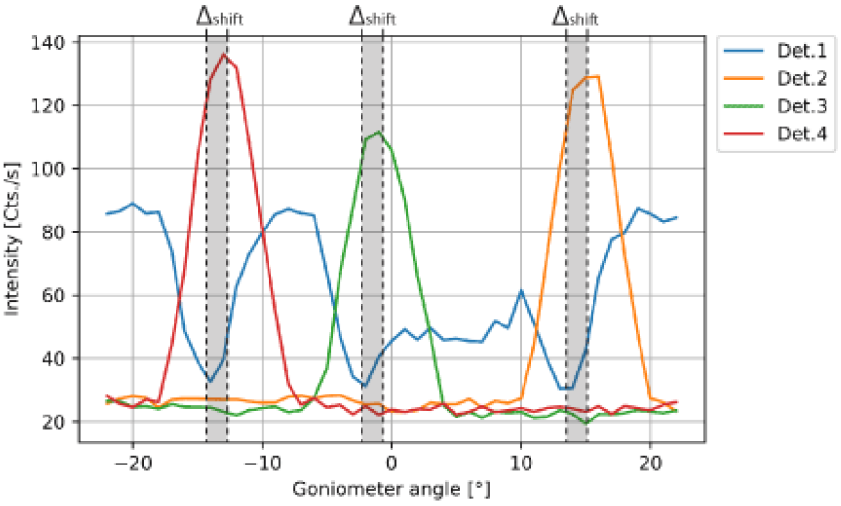

Figure 27: Diagram of an exemplary angle scan. The angle position of the goniometer is plotted against the total intensity integrated over the whole λ range.

The angle position of the goniometer is plotted against the total intensity integrated over all wavelength for the different detectors. Noticeable is a drop in the intensity of the transmission detector for angles between 0° and 10°, which can be explained by the absorption of a BF_3 detector that is mounted in the detector cradle but has not been used for the experiment. Furthermore it can be observed that the maxima of the front detectors are shifted with respect to the minima of the transmission detector. The reason for this unexpected behaviour is identified as a misalignment of the transmission detector, which is mounted in a shifted position from the optical axis of the neutron guide. The angle shift Δ_{shift} (marked in fig. 27) has been determined by a gaussian fitting to the peaks of the front detectors and valleys of the transmission detector in the angle scan plots. The fitting has been performed on the peaks of detectors 2 and 4 and the correlated valleys of detector 1 for all four angle scans. This results in an angle shift $\Delta_{shift} = 1.57° \pm 0.13°$. With this information, the geometry of the detector assembly has been reconstructed as shown in fig. 28, resulting in a detector misalignment of 8.24 mm. The red marked space in fig. 28 indicates the area of the detector tube, that is located outside the optical acceptance of the neutron beam guide but still in the wavelength dependence acceptance region, given by the total reflection condition of the beam guide (see also ch. 6.1.3). The deviation of the detection efficiency due to this misalignment is $\leq 4\,\%$ approximated by the ratio between the full detector area given by the inner diameter of the detector tube and the red marked area shown in fig. 28. As shown in ch. 6.1.3 the acceptance angle increases and the detector is full covered by the beam with increasing λ of the neutrons. At around $\lambda \geq 3.75$ Å, the complete detector is illuminated.

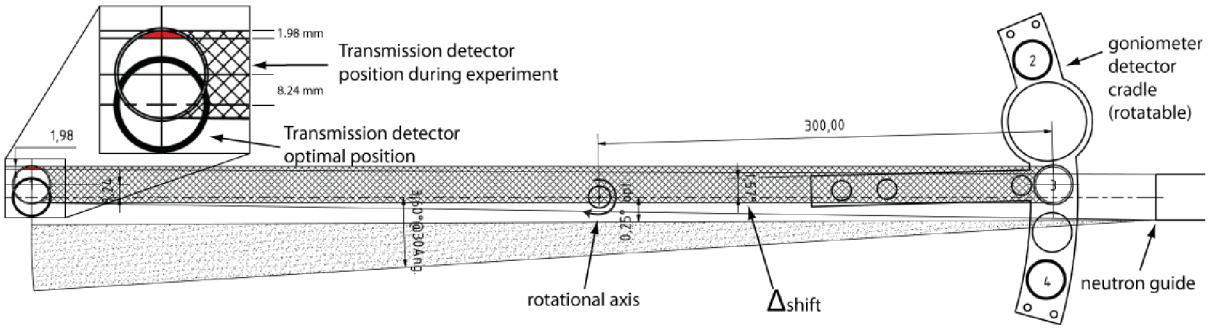

Figure 28: Drawing to scale of the detector assembly. The true position of the transmission detector 1 during the experiment has been determined by turning the goniometer for $\Delta_{shift} = 1.57°$ from 0° position.

5.4.1 VITESS 3.4 simulation

The corrected detector assembly geometry of the shading scenario described above has been simulated in VITESS 3.4, which is a ray-tracing based simulation software for neutron beamlines. A model has been constructed which takes the geometry of the detector and neutron guide positions and dimensions (see also ch. 4.6.1 and ch. 4.6) into account (fig. 29). Due to limitations of VITESS the tube detectors have been approximated with planar planes of ^{3}He with a width of 25.4 mm which is equal to the projected diameter of the ^{3}He detector tube and a height of 200 mm (length of the detector tube).

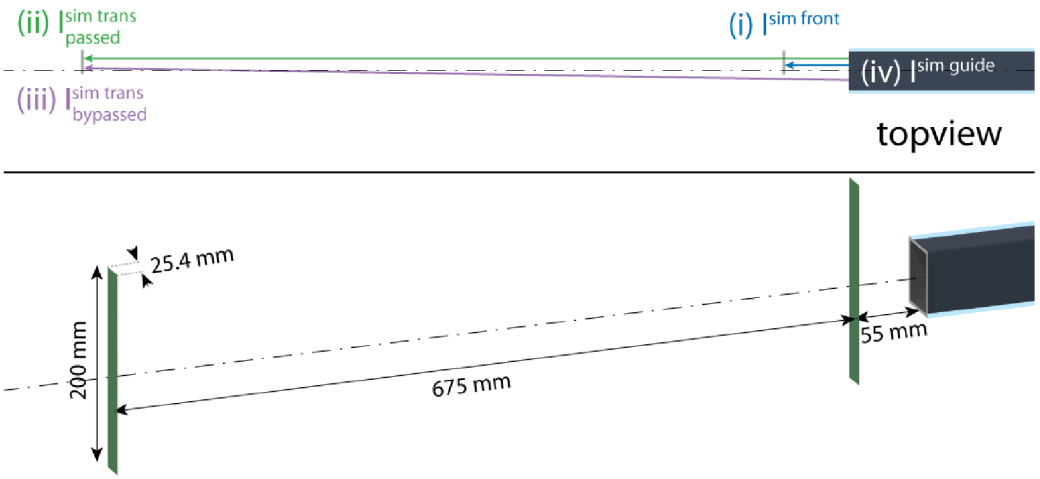

Figure 29: Sketch of the model used for the VITESS simulation with dimensions and distances true to scale. In the top view exemplary neutron paths for the three different cases of detection are depicted. The green transparent planes represents the active ^{3}He detectors for the VITESS simulation.

The position of the detectors are shift corrected for 8.24 mm from the optical axis of

the neutron guide following fig. 28. The inside of the neutron guide has the dimensions 7000 mm × 30 mm × 45 mm. A neutron source with homogenous energy spectra and homogeneous angle distribution in a range of 0 Å to 50 Å with a step size of $\delta = 0.05$ Å is placed at the surface of the mesitylene moderator and projected on the neutron guide entrance. The output of the simulation are five sets of neutron intensities depending on the wavelength in a range from 0 Å to 50 Å:

(i) intensity of the front detector $I^{sim\,front}$
(ii) intensity of the transmission detector from neutrons which passed through the front detector without being absorped $I^{sim\,trans}_{passed}$
(iii) intensity of the transmission detector from neutrons which bypassed the front detector $I^{sim\,trans}_{bypassed}$
(iv) intensity at the exit of the neutron beam guide $I^{sim\,guide}_{exit}$.
(v) intensity at the entrace of the neutron guide $I^{sim\,guide}_{entrance}$.

By normalising the detector intensities to $I^{sim\,guide}_{exit}$, three coefficients have been calculated:

$$a(\lambda) = \frac{I^{sim\,front}}{I^{sim\,guide}_{exit}}, \qquad b(\lambda) = \frac{I^{sim\,trans}_{passed}}{I^{sim\,guide}_{exit}}, \qquad c(\lambda) = \frac{I^{sim\,trans}_{bypassed}}{I^{sim\,guide}_{exit}}$$

These and the sum $b + c$ are plotted in fig. 30 with the same colour mapping for the three correlated neutron paths as shown in the topview of fig. 29. The wavelength dependence of a, b and c has been fitted by polynomial functions with a degree of 0 for a and a degree of 3 for b and c. Coefficient a is constant due to being placed close to the neutron guide exit and a high covering of the neutron guide window of ≈60 %. Coefficient b shows a decaying behaviour due to a wavelength dependend divergence (see eq. 17). The shape of curve c results also from the wavelength depended divergence. At small λ, the neutrons have a very small divergence and the transmission detector is not completely covered by the front detector. With increasing λ, the divergence increases allowing neutrons which bypass the front detector to hit the transmission detector. This results in a peak at ≈18 Å and afterwards a decay as with b. A calculation of ϵ_{det} based on these coefficients is described in the following section.

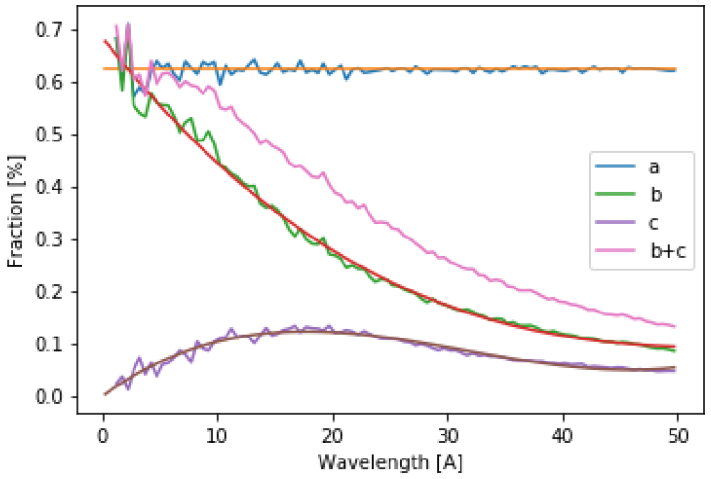

Figure 30: Plot of the normalised intensity data extracted from the VITESS 3.4 simulation against the wavelength λ and fitted with polynomial functions.

5.4.2 Calculation of the detector efficiency ϵ_{det}

For a calculation of the detector efficiency ϵ_{det}, the measured intensities and the simulation results obtained in the previous section are merged. Therefore, the spectra corresponding to the angle position of the peaks (front detectors) and valleys (transmission detector) shown in fig. 27 are plotted in fig. 31 for the shaded and not shaded transmission detector.

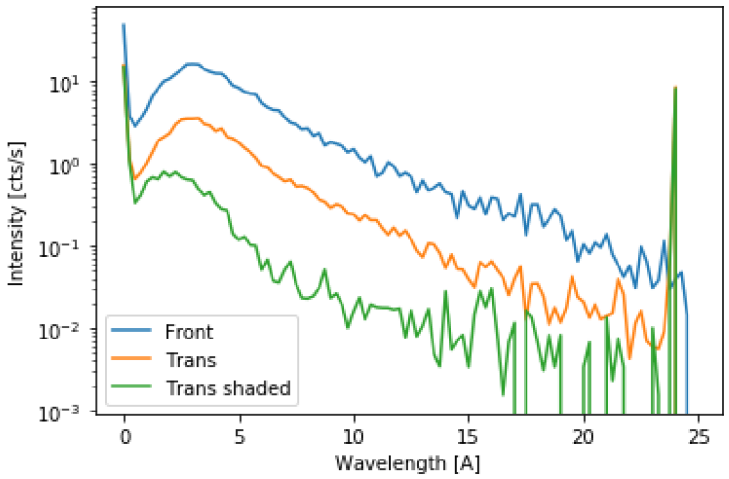

Figure 31: Averaged spectra over angle scan runs #68, #83 and #92 of the front detector 3 and the transmission detector 1 shaded and not shaded.

The previously presented coefficients a, b and c in ch. 5.4.1, generated by the VITESS 3.4 simulation, are instrumentalised to express the fluxes at the different positions to

the flux at the guide exit Φ^{guide}. Due to the normalisation to the simulated intensity at the neutron guide exit position $I_{exit}^{sim\,guide}$, the coefficients give unit less fractions, which take into account the detector dimensions, positions and different paths of the neutrons before absorption in the ^{3}He volume that represents the transmission detector. Therefore these coefficients can be used to express the flux at the back position Φ^{back} depending on the flux Φ^{guide} at the exit window of the neutron guide in the experiment.

$$\Phi^{back}(\lambda) = (b(\lambda) + c(\lambda)) \cdot \Phi^{guide}(\lambda) \tag{7}$$

The measured intensities for the shaded and unshaded case shown in fig. 27 $I_{shaded}^{trans}(\lambda)$ and $I_{unshaded}^{trans}(\lambda)$ can be connected with the absorption efficiency of ^{3}He ϵ_{He}^{det} using

$$\begin{aligned} I_{unshaded}^{trans}(\lambda) &= \epsilon_{He}^{det} \cdot \Phi^{back}(\lambda) \\ &= \epsilon_{He}^{det} \cdot (b(\lambda) + c(\lambda)) \cdot \Phi^{guide}(\lambda). \end{aligned} \tag{8}$$

Additionally it has to be taken into account that the stainless steel hull of the detector tube also absorbs neutrons which are thus not counted. Therefore eq. 8 has to be modified with a term consisting of the attenuation coefficient $\mu_{Fe}(\lambda)$ and the wall thickness of the detector tube t_{wall} which yields

$$I_{unshaded}^{trans}(\lambda) = e^{-\mu_{Fe}(\lambda)\cdot t_{wall}} \cdot \epsilon_{He}^{det} \cdot (b(\lambda) + c(\lambda)) \cdot \Phi^{guide}(\lambda). \tag{9}$$

The intesity in the shaded case can be expressed by the split fluxes at the transmission detector position Φ_{passed}^{trans} and $\Phi_{bypassed}^{trans}$ with

$$I_{shaded}^{trans}(\lambda) = \epsilon_{He}^{det} \cdot \left(\Phi_{passed}^{trans} + \Phi_{bypassed}^{trans}\right) \cdot e^{-\mu_{Fe}(\lambda)\cdot t_{wall}} \tag{10}$$

By using the VITESS coefficients in respect to the case "passed" or "bypassed" the split fluxes can be expressed in dependence of the flux at the neutron guide exit $\Phi^{guide}(\lambda)$. And also taking into account that neutrons which passed the front detector with a probability to be absorbed at two times the wall with

$$\Phi_{passed}^{trans}(\lambda) = b(\lambda) \cdot e^{-\mu_{Fe}(\lambda)\cdot 2w_{wall}} \cdot (1 - \epsilon_{He}^{det}) \cdot \Phi^{guide}(\lambda) \tag{11}$$

and

$$\Phi_{bypassed}^{trans}(\lambda) = c(\lambda) \cdot \Phi^{guide}(\lambda) \tag{12}$$

The measured intensity of the transmission detector $I_{shaded}^{trans}(\lambda)$ can also be expressed by inserting eq. 11 and 12 in eq. 10, resulting in

$$\begin{aligned} I_{shaded}^{trans}(\lambda) = &\epsilon_{He}^{det}(\lambda) \cdot \Phi^{guide}(\lambda) \cdot e^{-\mu_{Fe}(\lambda)\cdot t_{wall}} \\ &\cdot \left(b(\lambda) \cdot e^{-\mu_{Fe}(\lambda)\cdot 2t_{wall}} \cdot (1 - \epsilon_{He}^{det}) + c(\lambda)\right). \end{aligned} \tag{13}$$

The detection efficiency of the ^{3}He ϵ_{He}^{det} can be obtained by dividing eq. 13 by eq. 9. Solving to ϵ_{He}^{det} results

$$\epsilon_{He}^{det}(\lambda) = 1 - \left(\frac{I_{shaded}^{trans}}{I_{unshaded}^{trans}} \cdot \frac{b(\lambda) + c(\lambda)}{b(\lambda)} - \frac{c(\lambda)}{b(\lambda)} \right) \cdot e^{-\mu_{Fe}(\lambda) \cdot 2t_{wall}}. \tag{14}$$

The measured data (see fig. 31) and the VITESS generated coefficients (see fig. 30) are inserted in eq. 14.

This detector efficiency will be fitted with an analytically determined detector efficiency. The attentuation of a beam by a material with thickness l is given by $e^{-\mu \cdot l}$ with the attentuation constant μ. The absorption is therefore $1 - e^{-\mu \cdot l}$ as the number of particles scales linearly with the pressure p, this expression needs to be multiplied by $\frac{p}{p_0}$ with $p_0 = 1\,\text{bar}$ the "standard pressure". The absorption is therefore given by $1 - e^{-\mu \cdot \frac{p}{p_0} \cdot l}$. In order to get the absorption probability for a ^3He tube, the absorption needs to be averaged over all possible paths a neutron can take. As $l = 2 \cdot \sqrt{r^2 - x_i^2}$ with r the inner radius of the tube and x the distance from the center to the position within the tube, the absorption can be expressed with

$$\epsilon_{det}^{He}(\lambda, p) = \frac{1}{N} \sum_{i=0}^{N} \left(1 - e^{-\mu_{He} \cdot \frac{p}{p_0} \cdot 2 \cdot \sqrt{r^2 - x_i^2}} \right), \tag{15}$$

where the radius r is divided into N parts.

Unfortunately the experimentally determined ϵ did not show the expected behaviour which was the reason that the fit of the analytically determined ϵ yielded non-physically results. This is most likely due to the misalignment of the transmission detector. For the next experiment it would be wise to test this approach to determine ϵ by placing two detectors directly behind each other. The pressure p of the ^{3}He filling could not be obtained and verificated by utilising the measured neutron data. Therefore the pressure $p = 5\,\text{bar}$ specified by the manufacturer, is used in the following.

The efficiency of the detector tube can be calculated by eq.16, which combines the efficiencies of the ^{3}He gas filling $\epsilon_{det}^{He}(\lambda, p)$ with the absorption of the tube hull. Due to the unknown stainless steel alloy of the detector hull pure Fe has been assumed. Therefore the absorption can be slightly overestimated.

$$\epsilon_{det}(\lambda, p) = \epsilon_{det}^{He}(\lambda, p) \cdot e^{-\mu_{Fe}(\lambda) \cdot t_{wall}} \tag{16}$$

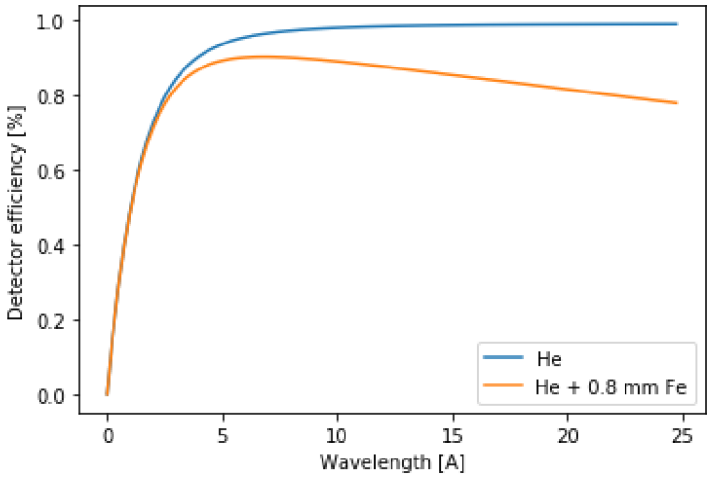

Figure 32: Detector correction curve calculated by eq. 16 with a pressure of $p = 5\,\text{bar}$ and a wall thickness of $t_{wall} = 0.8\,\text{mm}$.

In fig. 32 the detector efficiency, is plotted for the ^{3}He at a pressure of $p = 5\,\text{bar}$ and a Fe detector hull with a thickness $t_{wall} = 0.8\,\text{mm}$. The blue curve shows the detection efficiency $\epsilon_{det}^{He}(\lambda, p)$ of the ^{3}He filling of the detector. The orange curve combines the detector efficiency $\epsilon_{det}^{He}(\lambda, p)$ resulting from the absorption in ^{3}He and the absorption in Fe of the detector hull. The plots show that the absorption and therefore the detector efficiency of ^{3}He is rising for higher wavelengths and saturates in a plateau beginning from $\approx$4 Å at nearly 100 %, what underlines the superb neutron detection performance of ^{3}He. The combined efficiency of the detector which takes the absorption of the Fe hull into account shows a similar curve behaviour for small wavelengths but leads to a deviation at $\approx$4 Å with nearly linear decrease to $\approx$80 % for 25 Å. Therefore the influence of the tube hull on the detector efficiency is significant and cannot be neglected. The combined detector efficiency is used in ch. 6.1.4 to correct the neutron spectra data.

6 Data analysis

The data processing, correction and normalisation of the TOF spectra has been a main task of the experiment. Within the context of this thesis, a toolbox of python functions for the preparation, correction and analysis of TOF spectra data has been developed, which can also be used for following HBS experiments.

6.1 Correction of TOF data

6.1.1 Timing correction of neutron energy spectra

The timing correction of the data normalises the start time of different TOF spectra which is determined by an initial intense peak resulting from fast neutrons. The time of flight time frame is opened by a trigger pulse provided by the cyclotron which gives the information of the start of the proton pulse (see also ch. 4.6). The proton pulse correlates with the fast neutron pulse which is thermalised in the B-PE detector shielding and can therefore be detected. Due to technical reasons the trigger signal is delayed to the start of the proton pulse. Therefore the fast neutron peak appears split in P1 and P2 depicted in fig. 33. This has to be corrected which is explained in detail in the following.
The raw TOF spectrum measured with detector 3 is plotted in fig. 33. The maximum of $t_{fra} = 80.5\,ms$ represents the chosen length of the TOF time frame with a bin width of $t_{bin} = 25\,\mu s$. The overall time of acquisition was $t_{run} = 600\,s$ at a moderator temperature of $T_{mod} = 24\,K$.

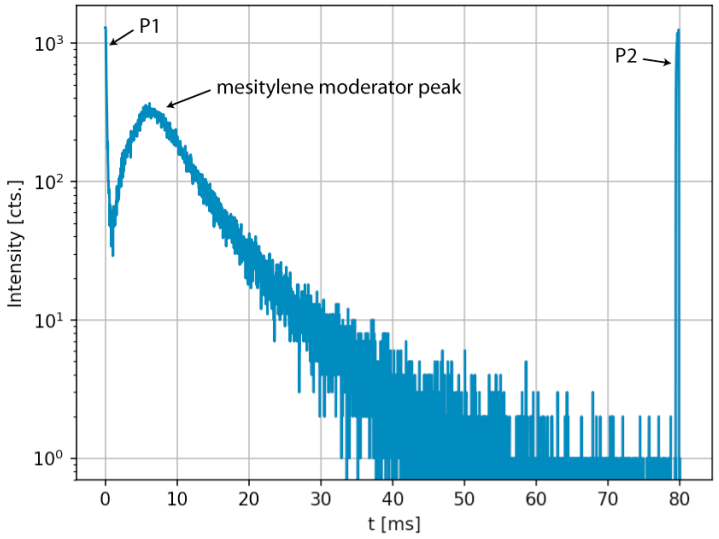

Figure 33: Raw TOF spectra of detector 3 measured at $T_{mod} = 24\,K$ with a run time of $t_{run} = 600\,s$, a frame length of $t_{fra} = 80.5\,ms$ and a bin width of $t_{bin} = 25\,\mu s$.

The plot in fig. 33 shows a sharp first peak (P1) at $t = 0$ ms which is given by fast neutrons. These neutrons originally produced in the target are predominately thermalised

in the B-PE detector shielding and reach the detector without passing the neutron guide as unwanted neutronic background which will be corrected in later steps. From $t = 1\,\mathrm{ms}$ the spectrum of the moderator setup including the PE volume of the thermal moderator is visible which is afterwards overlapped with the cold spectrum of the mesitylene moderator. It has a moderation peak at $t = 6\,\mathrm{ms}$ and a following decrease in intensity. A prominent feature of the spectra is the sharp peak at $t = 80\,\mathrm{ms}$. This second peak (P2) is a result of a delay between the trigger signal provided by the cyclotron and the start of the proton pulse. Therefore P2 represents the shifted start of the fast neutron peak and is shown magnified in the blue curve of fig. 35. Besides the neutron detectors, a pulse generator with a frequency of $f_{gen} = 4\,\mathrm{kHz}$ has been connected to an input of the TOF counter card to produce a constant reference count rate when the TOF time frame is open.

The generator signal has been utilised to apply two adjustments on P2, before it is shifted ahead of the spectra and combined with the P1. In the first modification the amplitude of the peak has to be upscaled due to the skipping of pulses resulting from the macro pulsing with period T_{mac} of the cyclotron (further explained in ch. 4.2). The TOF time frame is opened with a trigger signal continuously received in the micro pulse time period T_{mic}. With each period of T_{mac} the proton pulses are intermitted causing the open TOF frame to run to the maximum length t_{fra} and stop waiting for the next trigger pulse. When the next pulse triggers the TOF frame after the macro pulsing pause, the start of these fast neutron peaks (P2) are not counted due to the delay between trigger signal and arrival of the initial fast neutrons. The fraction of the missing counts can be determined by the ratio $R_{scale} = 1 - \frac{I_{after}}{I_{before}}$ of the averaged intensities before P2 (I_{before}) and after P2 (I_{after}).

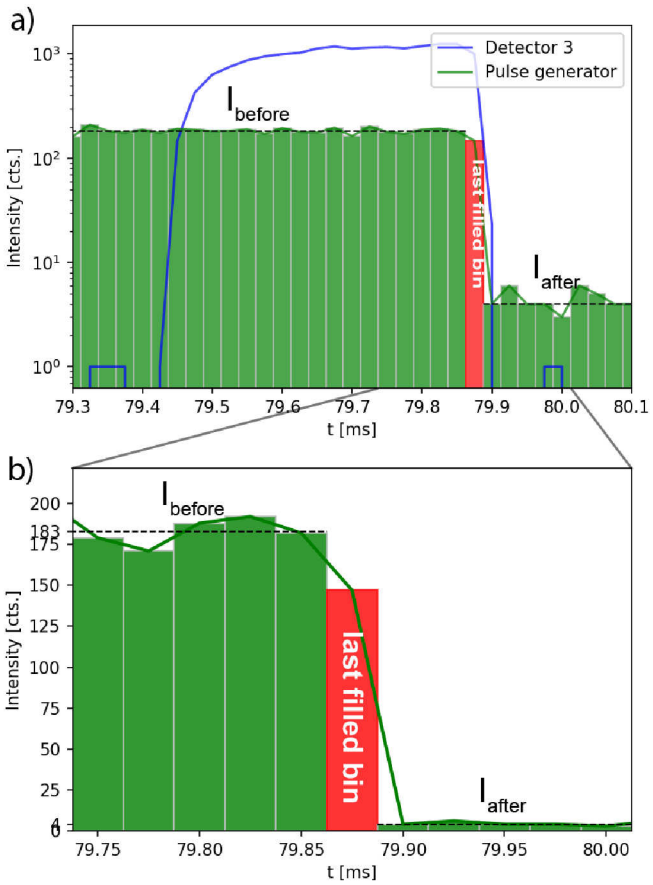

Figure 34: Bar plot of the pulse generator signal magnified for P2. The red marked bin shows the last, partially filled bin for TOF repetitions with T_{mic}. The dashed lines displays the average intensities before and after P2. In the semi logarithmic plot a) the blue line shows P2 measured by detector 3. b) shows the magnified area around the last filled bin.

A second modification is needed due to the fact that a reset of the TOF frame occurs mostly in between the grid points which are quantised with time period t_{bin}. To correct this effect, the counts which occurred in the last partial bin of the TOF frame (red marked in fig. 34) is distributed on the second peak by re-binning the detector data to a grid quantisation with t_{bin}. The ratio of the last partial bin length before the trigger signal and a complete bin length t_{bin} is determined by the ratio of intensity before P2 I_{before} and the bin where the falling edge of the pulse generator data occurs (last filled bin). This intensity ratio is equal to the time ratio of the partially bin length and one complete bin length. The raw data of P2 is plotted together with the rescaled and re-binned P2 in fig. 35.

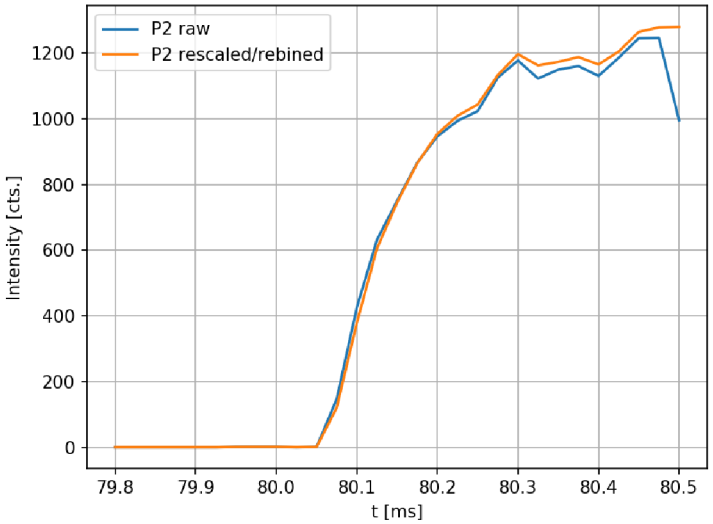

Figure 35: Magnified second peak P2 of raw spectra shown in fig. 33 combined with the rescaled data.

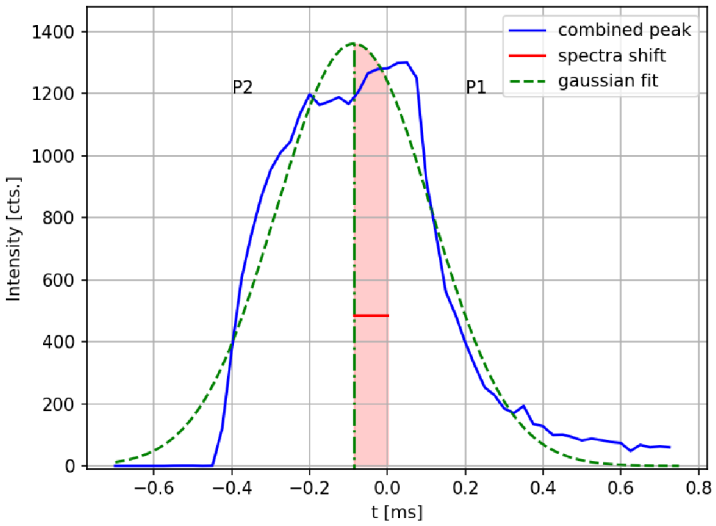

Figure 36: The plot shows P2+P1 magnified (compare also P1 in fig. 33 and P2 in fig. 35). A gaussian has been fitted to the resulting fast neutron peak.

Afterwards the rescaled and re-binned P2 is copied in front of P1 and results in the combined fast neutron peak presented in fig. 36. The center of a gaussian fitted to the fast neutron peak is defined as the start of the neutron spectra. The spectrum is shifted

as shown in fig. 36 and therefore normalised to the same starting time given by the gaussian center. The fast neutron peak characterised by the gaussian fit is also utilised for the calculation of the proton beam current which is described in ch. 6.1.5.

6.1.2 Background correction

After the determination of the fast neutron peak the background has to be subtracted. Therefore the detectors 2 and 4 are used which are placed beside the exit of the neutron guide.

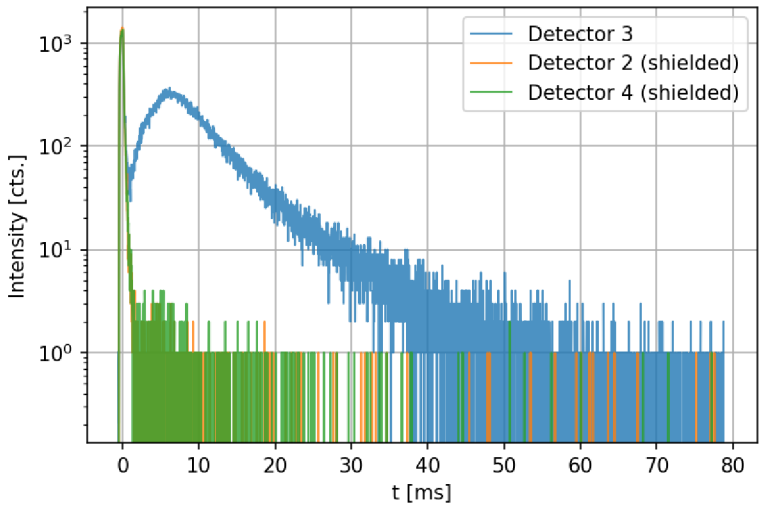

Figure 37: Rescaled and re-binned spectra of detector 3 which is placed in front of the neutron guide and detector 2 and 4 beside the neutron guide exit.

The rescaled and re-binned spectra are shown in fig. 37. It is obvious that compared to the spectra of detector 3, the moderated neutron distribution is missing in the spectra of detector 2 and 4, but the fast peak is prominent in all three spectra. A small amount of neutron counts can be observed at arrival times between $\approx$1 ms and $\approx$8 ms in the spectra of detector 2 and 4 resulting from fast neutrons which are backscattered inside the detector shielding. This points out that the fast neutron peak is mainly caused by fast neutrons which are thermalised in the B-PE shielding. The spectra of detector 2 and 4 which represents the neutronic background, is averaged and subtracted from the spectra of detector 3.

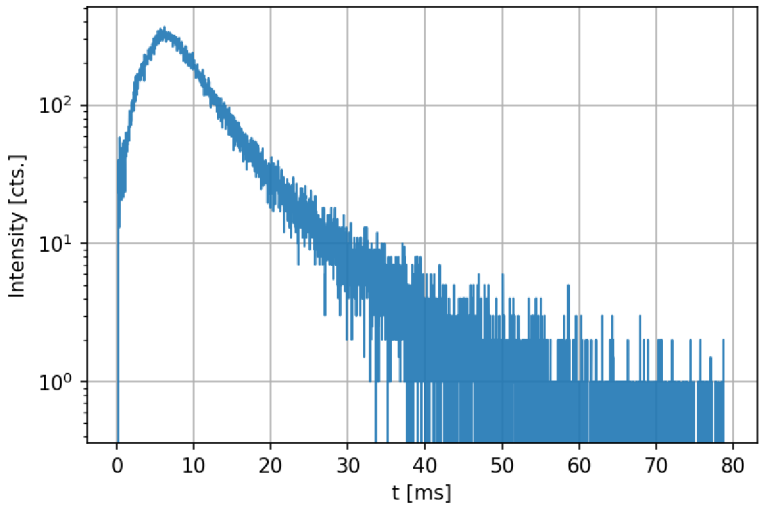

Figure 38: Corrected spectra after shifting and subtraction of neutronic background (raw data was shown in fig. 33).

The resulting spectrum is presented in fig. 38 which can be processed with the subsequent corrections presented in the following chapters.

6.1.3 Neutron guide acceptance correction

The influence of the neutron guide needs to be subtracted from the spectra to investigate the properties of the moderator system. The divergence of the neutron guide depends mainly on two contributions: (i) the divergence given by the geometry of the neutron guide (optical acceptance) and (ii) the wavelength dependent divergence given by the reflection properties of the guide.

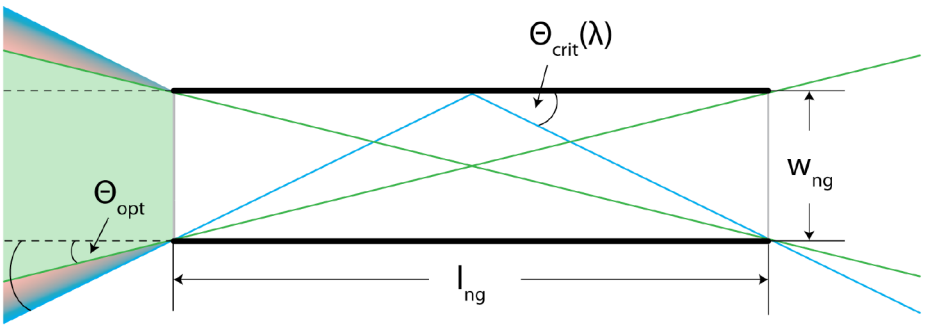

Figure 39: The top view sketch of the neutron guide shows exemplary (i) the divergence angle Θ_{opt} for the optical acceptance (green) and (ii) the wavelength dependent acceptance (color gradient from red for higher wavelengths to blue for lower wavelengths) given by the critical angle $\Theta_{crit}(\lambda)$.

$$\Theta^x_{opt} = arctan\left(\frac{w_{ng}}{l_{ng}}\right), \quad \Theta^y_{opt} = arctan\left(\frac{h_{ng}}{l_{ng}}\right) \tag{17}$$

Eq. 17 yields geometry depending divergence angles Θ^x_{opt} for the rectangular neutron guide with the inner dimensions of width w_{ng}, height h_{ng} and length l_{ng}. The optical acceptance (i) is depicted in fig. 39 as green marked area. From the dimensions of the neutron guide results $\Theta^x_{opt} = 0.25\,^\circ$ and $\Theta^y_{opt} = 0.37\,^\circ$.

The (ii) regime of acceptance is given by the condition for total reflection at the inner wall of the neutron guide. This is fulfilled for incident neutron beams with an angle $< \Theta_{crit}(\lambda)$ which can be expressed in good approximation with $\sin(\Theta_{crit}) \approx \Theta_{crit}$ by eq. 18 [6] with the reflection coefficient $m_{Ni58} = 1.2$ for a single coating with ^{58}Ni.

$$\Theta_{crit}(\lambda)[^\circ] \approx 0.1 \cdot m \cdot \lambda[\text{Å}] \tag{18}$$

The acceptance for the neutron guide is also shown true to scale in fig. 28 for Θ^x_{opt} and $\Theta_{crit}(\lambda = 30\,\text{Å})$.

To obtain a wavelength depending gain correction function for the characteristics of the neutron guide, a VITESS 3.4 simulation has been utilised analogous to the proceeding described in ch. 5.4.1. In this simulation the geometry of the neutron guide and the reflectivity properties[10] are taken into account. In front of the neutron guide input window, a neutron source with homogenous spectra and homogeneous angle distribution in a range of 0 Å to 50 Å with a stepsize of $\delta = 0.05$ Å is placed. The output of the simulation is the intensity $I_{in}(\lambda)$ at the entrance window and the intensity at the neutron guide exit $I_{out}(\lambda)$. Additionally a second simulation has been performed with the same parameters but a non reflective ("black") neutron guide. Therefore the wavelength independent fraction of the optical acceptance regime (i) has been isolated. The normalised intensity at the non reflective neutron guide exit $I_{out,black}$ is averaged to a scale factor S (eq. 19).

$$S = \frac{\overline{I^{out,black}}}{I_{in}} \tag{19}$$

$$\epsilon(\lambda) = \frac{I^{out}(\lambda)}{I_{in}(\lambda)} \cdot S^{-1} \tag{20}$$

Fig. 40 shows the simulated data points following eq. 20. This curve results from an overlay of the neutron guide divergence regimes (i) and (ii). To fit the data points a polynomial function with a degree of 6 has been chosen which is plotted as orange line. The polynomial fit function is applied on the measured spectra to correct the neutron guide characteristics.

[10] In the VITESS software, both the refractive index m and the roughness of the neutron mirrors are considered.

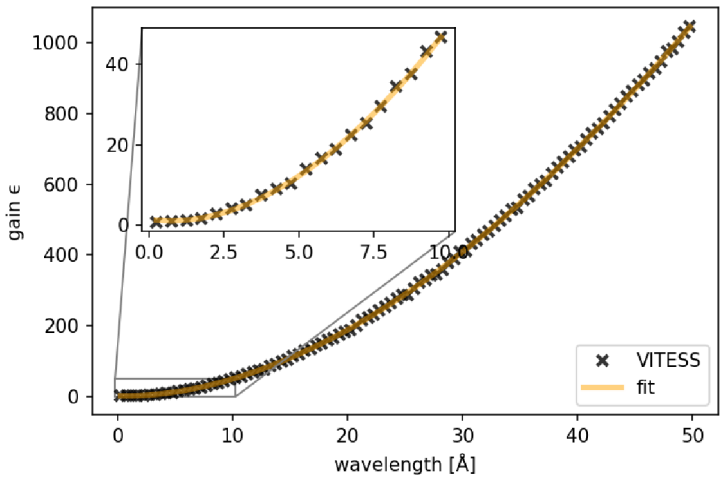

Figure 40: Diagram of the wavelength dependent gain of the neutron guide. The cross markers show the VITESS simulation datapoints, the orange line a fit with a polynomial of degree 6.

In fig. 41 the previously corrected example spectra (see also fig. 38) is plotted in blue. The orange curve shows the corrected spectra after applying the neutron guide gain $\epsilon(\lambda)$.

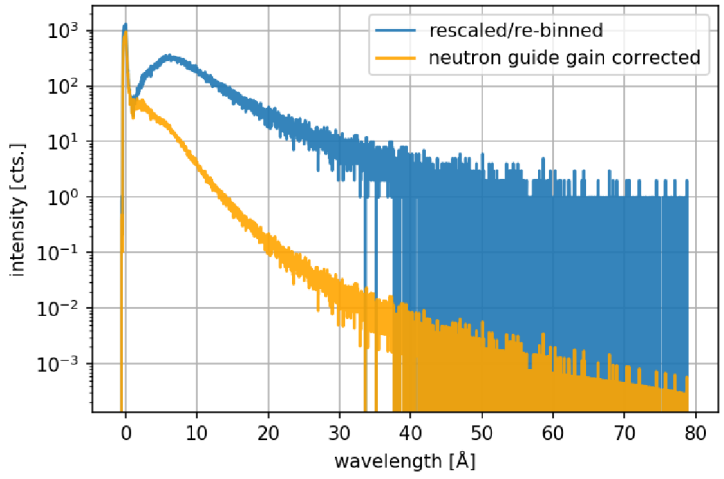

Figure 41: Rescaled and re-binned spectra (see also fig. 38) plotted in blue before correction and neutron guide gain corrected plotted in orange.

In the following the correction regarding the ^{3}He detector efficiency is applied to the neutron guide gain corrected spectra.

6.1.4 ^{3}He detector efficiency correction

To correct for the detector efficiency, the spectra shown in fig. 41 has to be divided by ϵ_{det} (as calculated in in ch. 5.4). Additionally, the TOF t can be converted to the wavelength λ using

$$\lambda(t)[\mathring{A}] = \frac{h \cdot t[ms]}{m_n \cdot l_{tof}[mm]} \cdot 10^{10} \tag{21}$$

with the planck constant h, the mass of the neutron m_n and the TOF path length l_{tof} introduced in ch. 4.6.4.

The now fully corrected spectra presented in fig. 42 represents the characteristics of the cold moderator system.

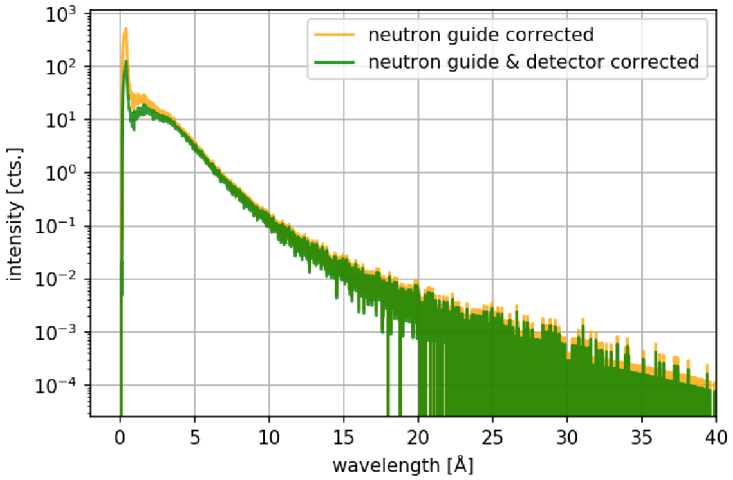

Figure 42: Rescaled, re-binned and neutron guide corrected spectra (see also fig. 41) plotted in blue before ^{3}He detector correction and after in green.

6.1.5 Reconstruction of p-beam current

The spectra need to be normalized to the proton beam intensity to compare different runs. Therefore the beam current has to be determined. During the COSY experiment investigating the mesitylene based cold moderator system, the target has been connected to a picoamperemeter attached to an analog-digital-converter (ADC) which logged the data in EPICS[11]. The data analysation after the experiment revealed that the logged data regarding the beam current could not be obtained for two reasons. (i) The sampling rate of the ADC and the log frequency of the EPICS system (10 Hz) was to slow to resolve the micro pulse time period T_{mic} and (ii) the baseline of the current measurement changed significantly over time. Therefore, a method has been developed to reconstruct retroactive the missing current data of the mesitylene experiment from the neutron data. After the mesitylene experiment, a sequent experiment regarding the investigation of a

[11] Experimental Physics and Industrial Control System

liquid hydrogen based cold moderator system has been performed in january 2020 at the Big Karl experimental hall (experiment "lH_2") in which the same target and detector setup has been used. The beam current has been measured by a picoamperemeter which amplifies and converts the current in a proportional voltage. In contrast to the mesitylene experiment, this signal has been preprocessed by a RedPitaya[12] as shown in fig. 43 before it has been logged in EPICS. The algorithm programmed in the RedPitaya integrates the current of every proton pulse and the background in between these pulses in a timing scheme of 1 ms integration time of the pulse, 1 ms pause to ensure that the pulse has ended and 1 ms integration time for the background. This ensures that a baseline change does not influence the current measurement thus resulting in a correct current determination. Due to the preprocessing, the integrated current data for a run can be obtained by retrieving the last integrated value U_{pulse}^{last} and the last integrated background value U_{bg}^{last} for this run.

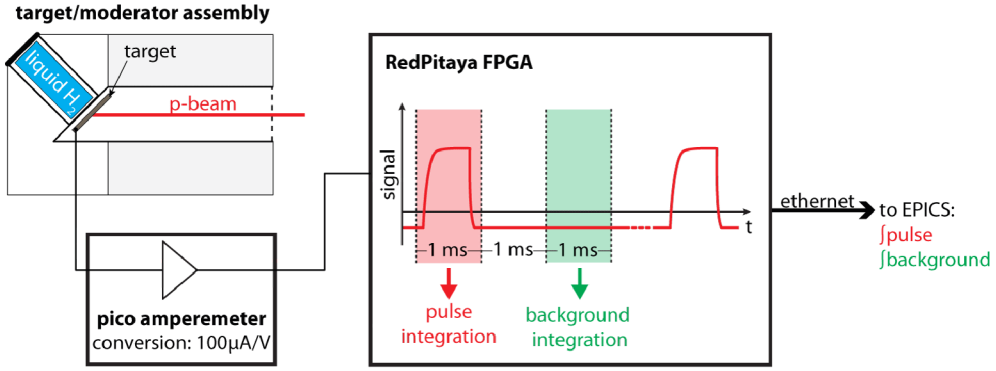

Figure 43: Sketch of the current measurement setup used since the second half of the experiment "lH_2 moderator". The Ta target is connected to a picoamperemeter to amplify and convert the current to a proportional voltage signal. The signals of proton pulse and background are separately integrated by a RedPitaya FPGA and stored in EPICS.

The proton intensity I_p for one run can be calculated by

$$I_p[cts.] = \frac{(U_{pulse}^{last} - U_{bg}^{last}) \cdot C_{sens}}{e} \tag{22}$$

with the sensitivity factor of the picoamperemeter $C_{sens} = 100\,\mu A\,V^{-1}$ (sensitivity range 6) and the elementary charge e. Following eq. 22, the proton count for the runs of the experiment "lH_2" has been calculated and plotted in fig. 44.

[12]FPGA (Field Programmable Gate Array) data acquisition system

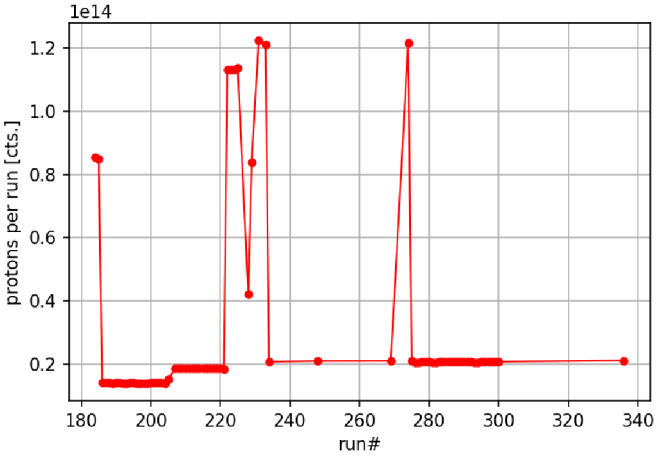

Figure 44: Plot of the measured proton beam current I_p against the run# of the experiment "lH_2".

As shown in ch. 6.1.1, the amount of neutrons in the fast neutron peak of a spectrum results from neutrons which are moderated in the B-PE shielding. Thus, these fast neutrons measured by the shielded detectors 2 and 4 (fig. 37) is independent from properties of the moderator system but proportional to the number of protons, which can be determined by integration of the gaussian fitted to the rescaled, rebinned and combined fast neutron peak (see also fig. 36). The fast neutron intensity I_{fn} of a run is defined as the average of the integrated fitted gaussians of the shielded detectors 2 and 4 which is plotted in fig. 45.

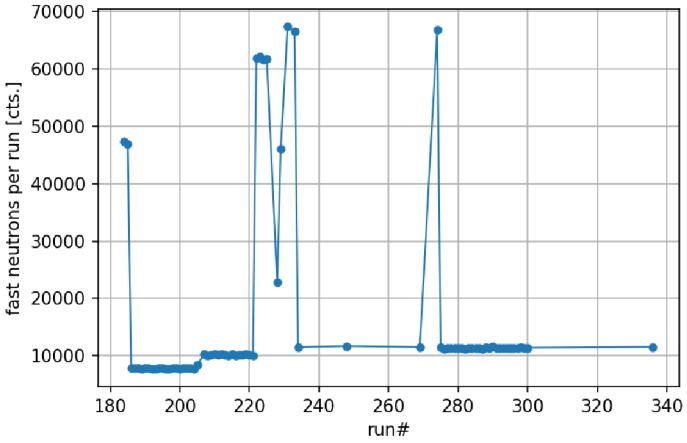

Figure 45: Plot of the fast neutron intensity I_{fn} against the run# of the experiment "lH_2".

The comparison of fig. 44 and fig. 45 shows a very good correlation between the

p-beam current and the fast neutron intensity which points out that the fast neutron data can be used to determine the proton current also for the "mesitylene" experiment. The conversion factor $C_{conv} = \frac{I_p}{I_{fn}}$ is calculated by averaging over every run of the experiment "lH_2" and plotted in fig. 46.

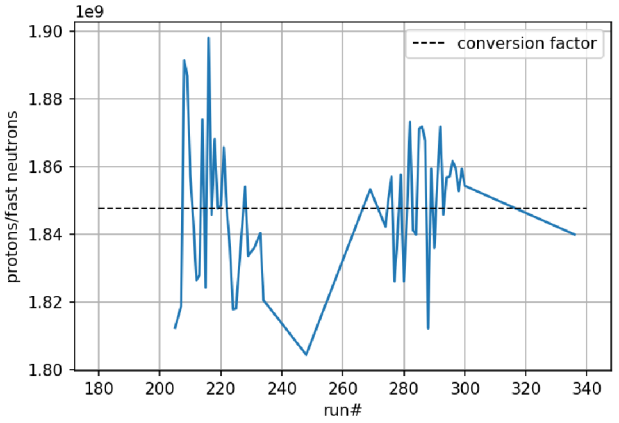

Figure 46: Plot of the quotient I_p/I_{fn} against the run# of the experiment "lH_2". The dashed line shows the conversion factor C_{conv}.

The conversion factor is determined to $C_{conv} = 18.5 \cdot 10^8 \pm 0.2 \cdot 10^8$ with an uncertainty of $\approx 1\,\%$. With the help of C_{conv}, the proton pulse intensity I_p can be calculated for the "mesitylene" experiment by converting I_{fn}. The proton intensity I_p normalised to the runtime of each run t_{run} is presented in fig. 47.

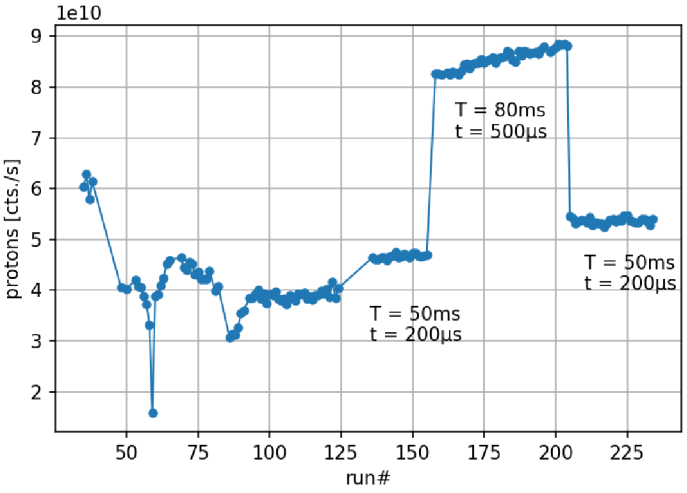

Figure 47: Plot of I_p calculated from I_{fn} normalised to the runtime t_{run} regarding the run# of the experiment "mesitylene".

The normalised proton intensity allows to identify the change of the beam parameters T_{mic} and t_{pulse} and therefore the duty cycle of the beam from $\frac{200\,\mu s}{50\,ms} = 0.4\,\%$ to $\frac{500\,\mu s}{80\,ms} = 0.625\,\%$ for the runs from #158 to #207 as labelled in the plot.
It has been shown that the new developed current measurement technique for the "lH_2" experiment can give reliable information about the beam current and can be correlated to the fast neutron data in the "mesitylene" experiment to reconstruct the beam current from this data. Therefore the obtained conversion factor C_{conv} is used in ch. 6.2 to rescale the neutron spectra with the beam current I_p.

6.2 Interpretation of data

To investigate the data obtained in the experiment, the runtime of each single run at the same mesitylene temperature is summed up and shown in tab. 1.

T_{mod} [K]	t_{run} [s]	f_{pulse} [Hz]	T_{mic} [ms]
22	3260	20	50
30	8400	20	50
40	7200	20	50
52	5400	20	50
57	6000	20	50
90	5400	20	50
100	3300	20	50
140	4200	20	50
180	3300	20	50
300	1890	33	30.3

Table 1: Overview of the total run time t_{run} at each mesitylene temperature T_{mod} and the pulse frequencies f_{pulse} with the corresponding micro pulsing time period T_{mic}. The pulse width have been $t_{pulse} = 200\,\mu s$ for all measurements. The data is measured with detector 3 and a bin width of $t_{bin} = 25\,\mu s$

Fig. 48 shows the measurements for moderator temperatures T_{mod} between 300 K to 22 K with full applied data correction as explained in the previous chapters.

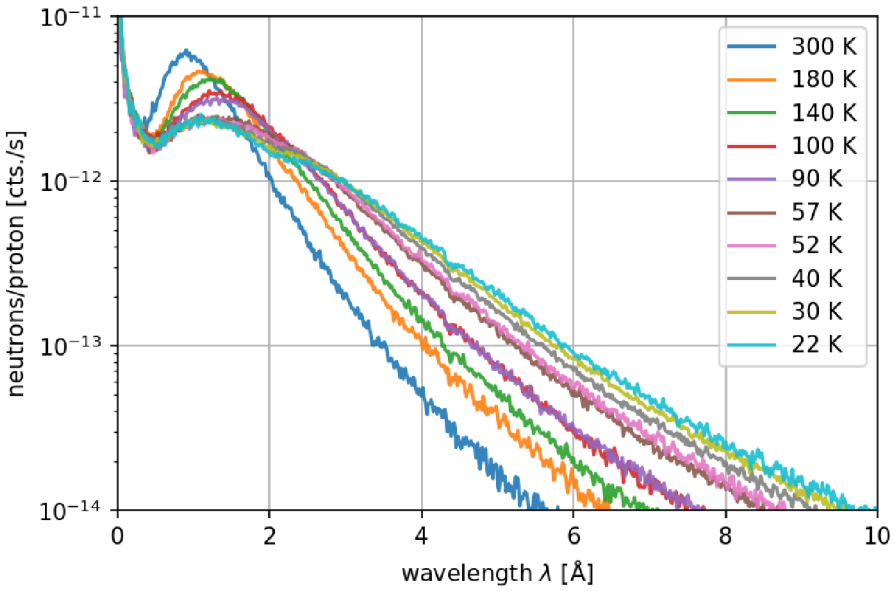

Figure 48: Spectra of the summed up and corrected runs for mesitylene temperatures T_{mod} in a range from 300 K to 22 K.

At all moderator temperatures, a strong asymptotic increase of the intensity I(λ) can be observed as the wavelengths approaches 0 Å. Moving to higher wavelengths, first a minimum in I(λ) is obtained which shifts from $\approx$0.3 Å at 300 K to $\approx$0.5 Å at 22 K, followed by a local maximum at increasing values of λ and broader peak width for decreasing temperatures.

Near 0 Å, high-energy neutrons pass the mesitylene nearly unmoderated, leading to the asymptotic behaviour at low wavelengths. At higher wavelengths, the neutrons start to interact with the cold moderator, which results in temperature dependent I(λ).

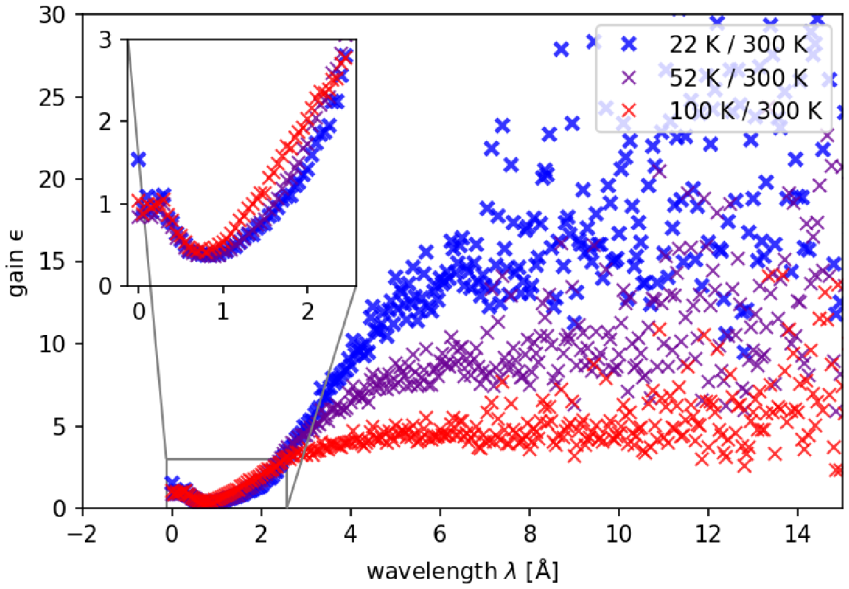

Figure 49: Intensity gain factor ϵ for 22 K, 52 K and 100 K normalised to the room temperature spectrum (300 K) plotted in dependence of λ. The inset shows the low λ region.

The spectra can be further investigated by comparing (i) the gain factor and (ii) the neutron temperature T_n at $T_{mod} = 22$ K, 52 K and 100 K. The neutron temperature T_n corresponding to the wavelength λ is calculated following

$$T_n(\lambda) = \frac{h^2}{2k_B \cdot m_n \cdot \lambda^2} \quad [1] \tag{23}$$

with the planck constant h, the neutron mass m_n and the Boltzmann constant k_B.

Fig. 49 shows spectra at $T_{mod} = 22$ K, 52 K and 100 K normalised to the room temperature measurement at 300 K.

At low wavelengths between 0 Å and 0.8 Å, the gain is independent of the moderator temperature as can be seen in the inset. The moderator at 300 K gives the best performance here which is also visible in the dip at 0.8 Å. For $\lambda \leq 0.8$ Å the gain increases stronger for $T_{mod} = 100$ K compared to lower T_{mod}. This behaviour changes at ≈ 2.5 Å when the gain for $T_{mod} = 100$ K pass into a saturation. For lower T_{mod} a gain saturation is reached at higher values. Tab. 2 lists the saturation position λ_{sat} for specific T_{mod} together with the respective neutron temperatures T_n and gain factors ϵ.

T_{mod} [K]	λ_{sat} [Å]	T_n [K]	ϵ
22	5.5	21	19.0 ± 2.2
52	4	40	11.0 ± 0.9
100	2.5	101	5.0 ± 0.4

Table 2: λ_{sat} and T_n where the gain factor ϵ converges into saturation.

In fig. 50 the neutron yield for wavelength of interest 1 Å, 2.5 Å and 5 Å is plotted against the moderator temperature T_{mod}. The wavelengths are chosen regarding different possible applications for cold neutrons (5 Å) and thermal/epithermal neutrons (2.5 Å and 1 Å). The regions of interest have been extracted from the spectra data (fig. 48) in an interval with a width of $\Delta\lambda = 0.5$ Å around the wavelengths and averaged.

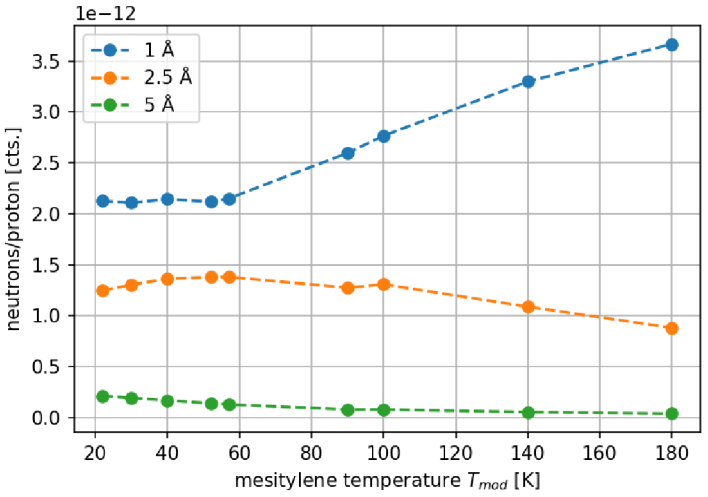

Figure 50: Intensities for wavelength of 1 Å, 2.5 Å and 5 Å plotted for different moderator temperatures T_{mod} extracted from the spectra presented in fig. 48.

For higher energetic neutrons at 1 Å the intensity decreases with decreasing mesitylene moderator temperature T_{mod}. A plateau occurs between 22 K and 57 K. Upon lowering T_{mod}, neutrons from the 1 Å population are moderated to longer wavelengths. As the 2.5 Å population exhibits a higher increase in neutron yield, it is assumed that a higher amount of neutrons are moderated to 2.5 Å compared to 5 Å. In the 2.5 Å population a intensity peak can be observed at $T_{mod} = 50$ K and can therefore serve as operation point of the moderator system to be used in bispectral applications. Also cold neutrons (5 Å at $T_{mod} = 22$ K) can be provided with a sufficient intensity for an appropriate instrumentation (see also ch. 2).

The neutron yield in dependence of its temperature T_n can also be described by the Maxwell-Boltzmann statistics, which originates from a thermodynamical description of the velocity distribution of particles in an ideal gas model.

Due to the moderation process of free neutrons which interchange kinetic energy mainly by elastic collisions, the kinetic energy distribution can be approximated by the model of an ideal gas in which other interactions than elastic energy exchanges between

the particles are neglected [8]. Therefore the Maxwell-Boltzmann distribution can be modified by inserting the corresponding neutron temperature T_n instead of the velocity of the neutrons, as given in eq. 24 with the amplitude N for the neutron population, the neutron mass m_n and the Boltzmann constant k_B.

$$I = \frac{N}{\lambda^4 \cdot \sqrt[3]{T_n}} \cdot \mathrm{e}^{\frac{-h^2}{2m_n \cdot \lambda^2 \cdot k_B \cdot T_n}} \tag{24}$$

A sum of three Maxwell-Boltzmann functions is fitted regarding the populations $N_{0,1,2}$ and the neutron temperature of the distributions $T_{0,1,2}$ to the spectra data shown exemplary for $T_{mod} = 140\,K$ in fig. 51. The three distributions are chosen to separate neutron populations resulting from different grades of moderation into:

N_2: Epithermal neutrons which have undergone just a few moderation interactions.
N_1: Thermal neutrons mainly interacted with the PE thermal moderator.
N_0: Cold neutrons which had interactions with the mesitylene of the cold moderator.

The temperature distribution resulting from the moderation process can approximately be reproduced by eq. 24 although it has to be considered that a demand of the Maxwell-Boltzmann distribution is the thermal equilibrium of the particles. An inverse term with an amplitude A and a power b is added to fit the decay of the high energetic fraction of neutrons which does not or slightly interact with the moderators and is therefore independent from T_{mod} (see also fig. 49).

$$I = \frac{A}{\lambda^b} + \sum_{i=0}^{3} \frac{N_i}{\lambda^4 \cdot \sqrt[3]{T_{n,i}}} \cdot \mathrm{e}^{\frac{-h^2}{2m_n \cdot \lambda^2 \cdot k_B \cdot T_{n,i}}} \tag{25}$$

Eq. 25 has been fitted to the spectra with the fit parameters A and b, as well as $N_{0,1,2}$ and $T_{0,1,2}$ as the amplitude and neutron temperature for three different populations, respectively. The fitted spectrum is shown exemplary in fig. 51 for $T_{mod} = 140\,\mathrm{K}$.

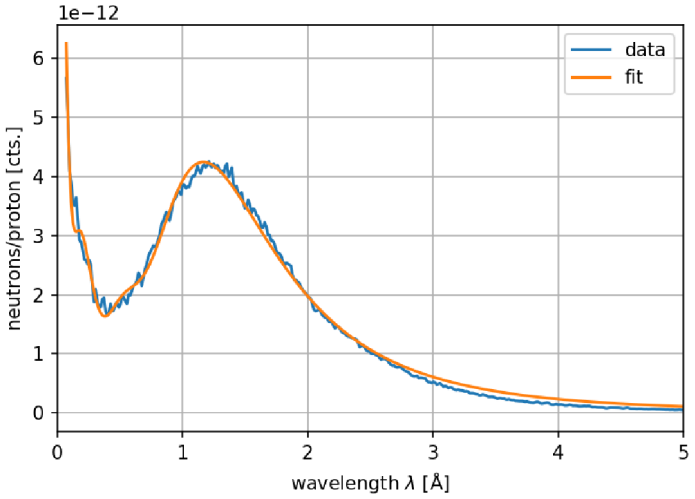

Figure 51: Spectra at a moderator temperature $T_{mod} = 140\,\mathrm{K}$ fitted with eq. 25.

The neutron populations $N_{0,1,2}$ of the distributions obtained from the fits for all spectra are plotted in dependence of the cold moderator temperature T_{mod} in fig. 52, the neutron temperatures $T_{0,1,2}$ of the distributions in fig. 53. It can be seen that the population N_0 decreases for $T_{mod} \leq 180\,\mathrm{K}$ whereas N_1 increases. Upon decreasing T_{mod}, the population N_2 is nearly constant with T_{mod} between 180 K and 22 K, with a value of 3000 cts Population N_1 increases by a factor of 2.8, from $\approx 10\,000$ cts to $\approx 28\,000$ cts. In contrast, N_0 decreases by a factor of 2.6 of its maximum value, from $\approx 64\,000$ cts to $\approx 25\,000$ cts.

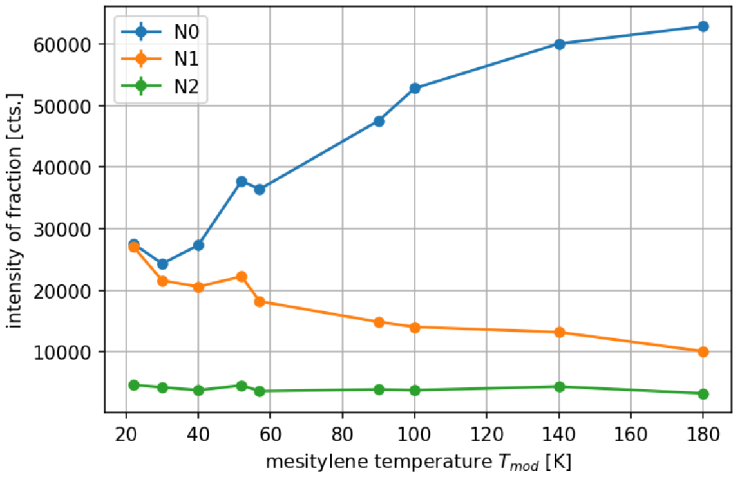

Figure 52: Intensities of the different neutron populations of the three Maxwell-Boltzmann distributions obtained by fitting to measured spectra (fig. 48) of frozen mesitylene ($T_{mod} \leq 180\,\mathrm{K}$) and plotted in dependence of T_{mod}. The fit errors are fully covered by the size of the markers.

In fig. 53 it can be seen that with decreasing T_{mod} the average temperatures T_0, T_1 and T_2 decrease approximately linear with different rates $\frac{\partial T_0}{\partial T_{mod}} < \frac{\partial T_1}{\partial T_{mod}} < \frac{\partial T_2}{\partial T_{mod}}$.

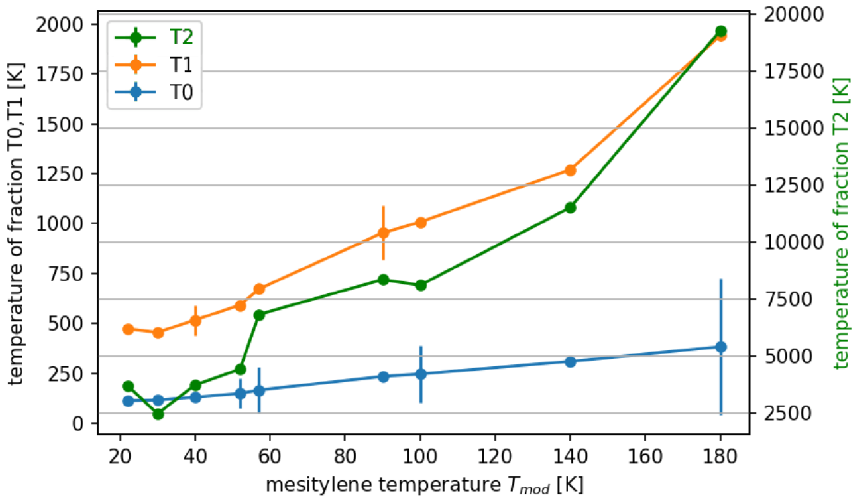

Figure 53: Average neutron temperatures of the different neutron populations of three Maxwell-Boltzmann distributions obtained by fitting and plotted in dependence of T_{mod}.

The decreasing occupation of N_0 and increasing occupation of N_1 is caused by the broadening of the mesitylene moderator peak of the spectra with lower T_{mod}. The energy of a transfer is mostly a function of the initial energy of a neutron. Therefore the energy transfer is highest for higher population temperatures. This shows that N_1 is far away from a thermal equilibrium and results most likely from the thermal PE moderator whereby N_0 results mostly from the mesitylene moderator. The higher difference between T_1 and T_{mod} compared to T_0 and T_{mod} results in a higher energy transfer between the neutrons of population N_1 (with T_1) and the mesitylene. In comparison to N_0 and N_1 is N_2 on a low constant level and represents a small population of less moderated neutrons.

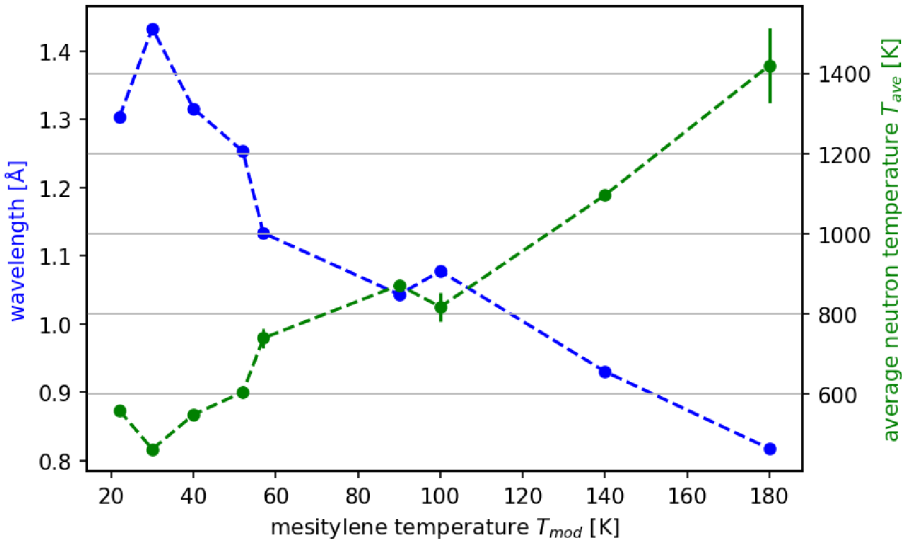

Figure 54: Weighted average neutron temperature and corresponding wavelengths of the three Maxwell-Boltzmann distributions plotted in dependence of T_{mod}.

The average temperature T_{ave} resulting from $T_{0,1,2}$ weighted by the amount of neutrons in the respective populations $N_{0,1,2}$, is plotted together with the corresponding λ in dependence of T_{mod} in fig. 54. The average neutron temperature T_{ave} shows the trend of a linear relation to the cold moderator temperature T_{mod} over the whole range from 22 K to 180 K. T_{ave} gives information about the moderation properties of the whole moderator setup, the temperature of the population T_0 mainly represents the moderation properties of the cold mesitylene moderator. The quotient $q = \frac{T_0}{T_{mod}} - 1$ is a figure of merit for the grade of undermoderation of the cold moderator system. An overview of the evaluated temperatures and the grade of undermoderation is given in tab. 3. For $T_0 = T_{mod}$ it holds $q = 0$ and the neutrons are fully moderated.

T_{mod} [K]	T_{ave} [K]	T_0 [K]	q [%]
22	559 ± 2	115 ± 1	423 ± 7
30	462 ± 2	118 ± 1	292 ± 5
40	548 ± 10	132 ± 1	230 ± 3
52	605 ± 15	151 ± 75	190 ± 145
57	739 ± 24	168 ± 116	194 ± 205
90	872 ± 10	236 ± 1	162 ± 2
100	818 ± 36	248 ± 144	148 ± 144
140	1096 ± 3	312 ± 1	123 ± 1
180	1421 ± 94	384 ± 343	114 ± 191

Table 3: Overview of the moderator temperatures T_{mod}, the average neutron temperature T_{ave}, the temperature of the population T_0 and the grade of undermoderation q.

With higher q the difference between T_{ave} and T_{mod} increases and the system is

more undermoderated. The lower T_{mod} the higher is the undermoderation of the cold moderator system. That indicates that either the moderator volume is to thin so that no thermal equilibrium can be achieved or that this has a too large contribution from the thermal moderator (PE) volume.

7 Conclusion & outlook

In this thesis the results of the investigation of the performance of a mesitylene based cold moderator system at moderator temperatures in a range of 22 K to 300 K are presented. The experiment has been performed at the Big Karl experimental hall of the COSY facility, Forschungszentrum Jülich GmbH. The JULIC cyclotron accelerator provided a 45 MeV proton beam to produce neutrons in a Ta(p,n) nuclear reaction. The neutrons have been pre moderated in a thermal PE moderator and moderated in the mesitylene cold moderator system. The mesitylene has been cooled by a coldhead cryocooler. Stable setpoints between 22 K to 180 K have been realised with a PID controlled counter heater setup. The moderated neutrons have been measured via TOF using a 7000 mm neutron guide as flight path and ^{3}He tube detectors in a TOF counter mode to measure the neutron spectra. To analyse and correct the obtained spectra, a python toolbox has been developed which functions give also a good base to analyse following moderator experiments.
The measured spectra have been analysed regarding the gain of cold neutrons for different moderator temperatures compared to a room temperature spectrum. It has been shown that the gain for cold neutrons reach saturation plateaus between a gain factor of 5.0 ± 0.4 for 100 K and 19.0 ± 2.2 for 22 K. The neutron flux for three different wavelengths of interest, 1 Å, 2.5 Å and 5 Å, in view of technical applications of the moderator system has been investigated. For 1 Å neutrons the intensity decreases for moderator temperatures between 180 K to 57 K from ≈3.8 cts/s to ≈2.2 cts/s and remains constant for temperatures ≤57 K. For 2.5 Å neutrons the intensity rises for temperatures between 180 K to 57 K to a maximum of ≈1.5 cts/s and slightly decreases for moderator temperatures ≤22 K. Also for cold neutrons with 5 Å an increase in intensity for decreasing moderator temperatures ≤180 K to ≈0.3 cts/s at 22 K could be observed.
In order to investigate the neutron moderation more detailed, a separation of the measured spectra into three different neutron populations regarding their neutron temperature and occupation following the Maxwell-Boltzmann distribution have been performed. The fits result in a set of three fractionated neutron populations $N_{0,1,2}$ associated with an average neutron temperature $T_{0,1,2}$ per population. N_2 with the corresponding T_2 is the fraction with high energetic neutrons which interact just slightly with the moderators.The decrease of N_0 with an increase in N_1 with lower T_{mod} is related to the broadening of the cold moderator spectra peak. Population N_0 therefore represents neutrons which are mainly interacting with the mesitylene. To investigate the moderation properties of the whole moderator system, the average of the temperatures $T_{0,1,2}$ weighted with the corresponding populations $N_{0,1,2}$ has been calculated. Although the uncertainty in the neutron temperature is quite high, the trend of a linear dependence between the moderator temperature and the averaged neutron temperature can be observed. The figure of merit $q = \frac{T_0}{T_{mod}} - 1$ has been introduced, which gives a percental value for the grade of undermoderation (respectively the deviation from the thermal equilibrium) of the cold moderator system. The grade of undermoderation q increases from (114 ± 7) % at a moderator temperature of 180 K to (423 ± 191) % at 22 K. Unfortunately the uncertainties in q propagated from T_0 are high for $T_{mod} = 52$ K, 57 K, 100 K and 180 K in these data points due to the amount of fit parameters which causes instabilities of the fit.

In the data analysis it was shown that mesitylene is a reasonable cold moderator material. The possibility to compare the here presented data with previously performed experiments is limited by the strong dependence of the moderator system´s efficiency on the geometry. The JESSICA experiment shown in ch. 3 based on a distinctly larger moderator volume which was designed for the ESS project therefore the results for the performance of this mesitylene moderator is not directly comparable with the data obtained in the experiment shown in this thesis. As shown in ch. 3, the JESSICA experiment offered information about the performance of mesitylene in comparison with other moderator materials.

Another mesitylene based cold moderator experiment has been lately performed by Tasaki et al. [28]. In this experiment the moderator dimension with a surface of 100 mm x 96 mm and a width of 25 mm is closer to the setup presented in this thesis (compare to ch. 4.5) but has still a larger surface with a slightly different geometry. On the left side of fig. 55, TOF spectra for different temperatures are shown. The comparison with the spectra in this thesis (see also fig. 48) results that the typical broadening and shift of the cold moderator peaks to longer wavelength with decreasing moderator temperature can be seen in both experiments. In [28] the moderator peaks for similar moderator temperatures are slightly shifted to longer wavelength compared to the spectra in this thesis. It seems that in [28] the contribution from the thermal moderator volume is stronger suppressed then in the here shown setup which might be attributed to the different geometry like the insertion of the cold moderator in an extraction channel. The cold moderator peaks for similar moderator temperatures are slightly shifted to longer wavelengths in the work of Tasaki et al. [28] compared to the spectra of this thesis.

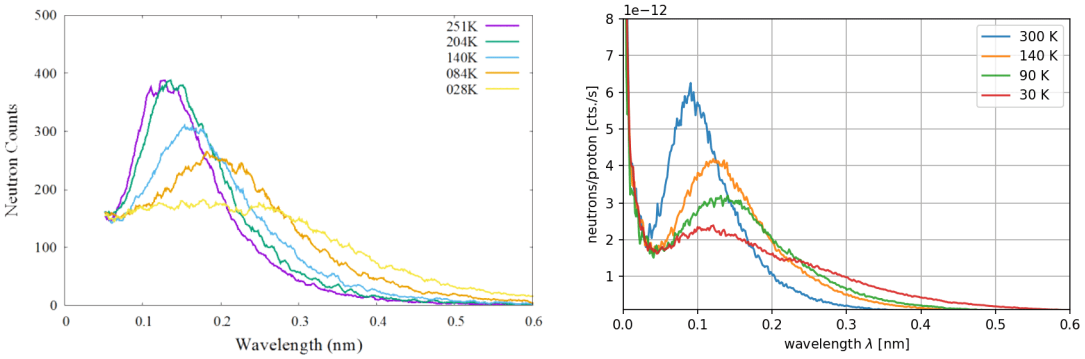

Figure 55: On the left side TOF neutron spectra for different moderator temperatures measured by Tasaki et al. are shown [28]. On the right side the neutron spectra presented in fig. 48 are plotted rescaled for a direct comparison.

The comparison regarding the relative moderator temperatures shows that the curve shape is in general similar but the gain factor is ≈2x higher in the here presented work (see fig. 49) compared to the results of Tasaki et al. given in fig. 56. It has to be considered that in the thesis results the spectra has been normalised to room temperature (300 K) whereby Tasaki et al. normalised to 251 K.

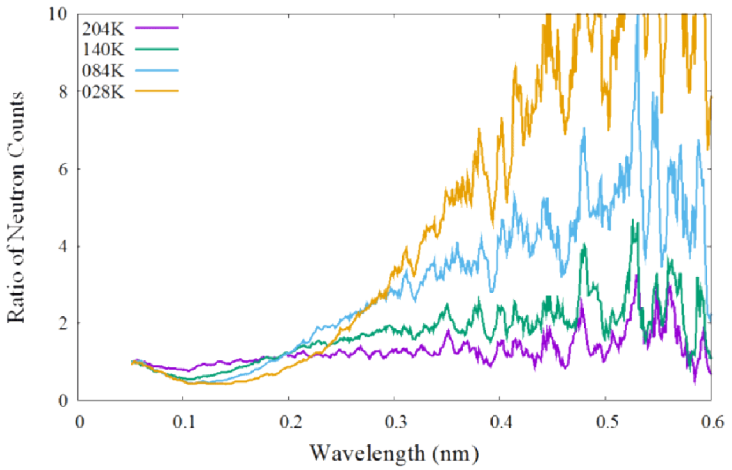

Figure 56: Relative neutron intensity for different moderator temperatures normalised to 251 K measured by Tasaki et al. [28].

Tasaki et al. has shown in [28] similar results in the moderating behaviour of mesitylene but the comparison has to be treated with caution even if the geometry of the moderator has been similar and the neutron production has been also performed by using a low energy nuclear reaction of a pulsed proton beam with a target material. Important differences in the setups are (i) the different thermal moderator volume and shape. (ii) The lower proton beam energy of 3.5 MeV and the use of a Be(p,n)-reaction [28] compared to a 70 MeV proton beam channelling a Ta(p,n)-reaction which produces a different initial neutron spectra and (iii) a different correction of the TOF spectra.

The comparison to other works show also that mesitylene is a moderator material with a good moderation efficiency whereby the performance of the moderator system is strongly depending on the technical design and geometry.

Outlook

The performance of the moderator system depends strongly on its geometry, therefore it cannot be directly compared to other moderator systems or concepts. With additional VITESS simulations the measured data can be further investigated regarding the brilliance B which is defined as:

$$B = \frac{neutrons}{0,1\% \frac{\Delta\lambda}{\lambda} \cdot Sr \cdot cm^2 \cdot s} \tag{26}$$

This definition describes the neutron current (number of neutrons per second) normalised to the radiant area and the solid angle of the emittance. Following Liouvilles theorem the volume in phase space is conserved for conservative movements[20]. Due to this the conservation of the brilliance of a source is the optimum and cannot being enhanced by any optical device. Therefore B is a meaningful figure of merit for the performance of a neutron source respectively moderator system. The calculation of the brilliance would allow to compare the cold moderator system with other moderator designs.

Regarding the cooling device as a central part of the cold moderator system, it has been shown that the presented cryo cooling setup was qualified to stabilise the mesitylene temperatures from 22 K to 180 K sufficiently to perform the measurements of the neutron spectra. Following experiments could be set up to investigate the moderation efficiency of mesitylene in different phase states. Therefore the setup has to be modified to enable a lower cooling rate in the temperature regime from the melting point at $T_{melt} \approx 228\,\mathrm{K}$ to the desired minimum temperature. This is needed to freeze mesitylene in the amorphous phase state II as explained in ch. 3 which promises a gain in the moderation efficiency. As explained in ch. 3 the performance of the system is strongly depending on the geometry of the moderator. The observed high undermoderation shown in ch. 6.2 can also be investigated in more detail and optimised with a larger moderator volume.
Due to the observed shrinking of the mesitylene during the freezing process described in ch. 5.2 it is promiscuous to do also further investigations here.

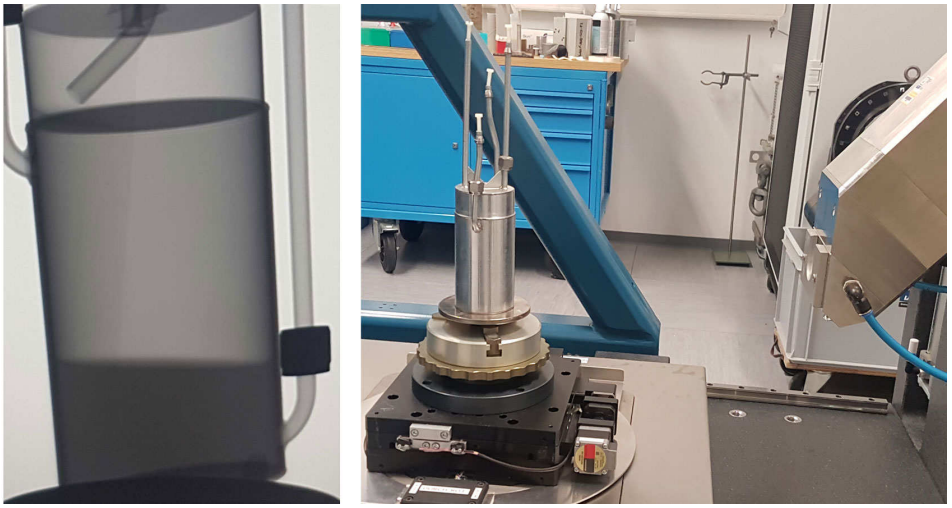

Figure 57: On the right side a x-ray image of an aluminium vessel half filled with liquid mesitylene is shown. A high contrast between mesitylene and air can be observed. The vessel is slightly tilted to identify the fill level. The left side shows the vessel on the sample stage of the x-ray system.

The vessel can be x-ray imaged to observe the homogeneous filling and freezing of the mesitylene. First approaches have been done with an x-ray system in cooperation with the ZEA-1 institute of Forschungszentrum Jülich GmbH. Fig. 57 shows an aluminium container filled with liquid mesitylene x-ray imaged It can be seen that it is possible to resolve a good contrast between liquid mesitylene and air at room temperature. The observation presented in ch. 5.2 regarding the outgasing of atmospheric gas leads to the assumption that (i) the change of the mesitylene density between the liquid and the frozen state is negligible and (ii) that voids can occur in the frozen mesitylene and reduce the moderator volume. From (i) follows that the contrast in x-ray imaging would be comparable also for frozen mesitylene and allow a further investigation of the vessel after freezing procedure to confirm a proper filling during the presented experiment afterwards. If (i) can be confirmed it follows that the construction of the cold moderator

can be improved. The mesitylene can be conditioned by using a vacuum to remove solved gases from the liquid before the vessel is filled. This could open the possibility to develop an encapsulated vessel which simplifies the construction significantly by waiver the closed loop system. The vessel has to be filled once and can be operated maintenance free.

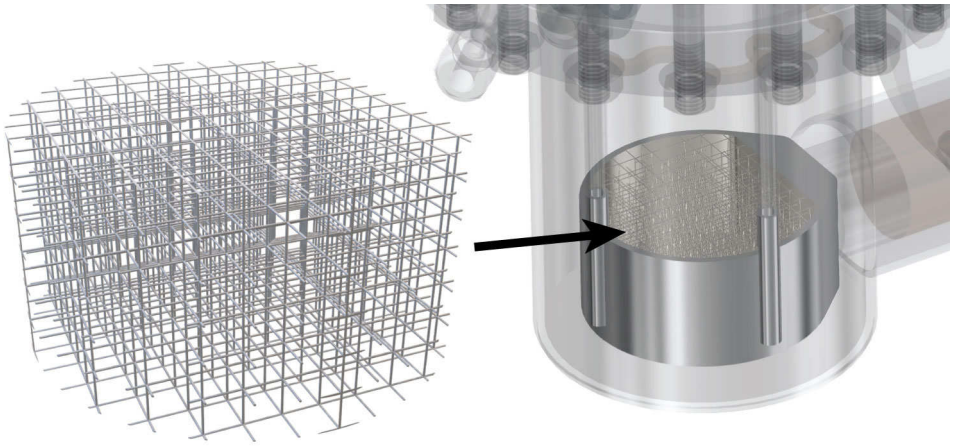

Figure 58: Conceptual design for an aluminium vessel inlay to serve as catalyst and heat distributor. The structure is a cuboid grid of rods with an edge length of 5 mm and a rod diameter of 0.3 mm.

Another upgrade of the moderator system can be achieved by an inlay grid inserted in the moderator vessel which is depicted in fig. 58 in a conceptual design. The structure can be manufactured from aluminium with the µ-SLS (Micro Selective Laser Sintering) 3D printing technique which is capable to reproduce feature sizes with sub-5 µm resolution [25]. This new component can enhance the moderator in two different ways: (i) As shown in ch. 3, organic compound based moderators degenerates due to the radicals formed in radiolyses processes. Mesitylene is less affected then other compounds but has still a limited lifetime in high neutron fields. This issue can be encountered by the use of aluminium as a catalyst suggested by Parajon et al. [22]. The proposed inlay benefits thereby from the typical rough surface structure resulting from the SLS process, which enlarges the catalytic capability. (ii) the heat distribution in the mesitylene with a low thermal conductivity is enhanced by the highly thermal conductive aluminium rods of the inlay and leads to a more homogeneous freezing. A disadvantage of the inlay is the reduction of the mesitylene volume which is ≈5.6 % for the exemplary shown structure. This loss can be reduced by an optimised inlay structure and exhausting the possibilities in resolution of new 3D printing techniques or counter measured by increasing the moderator volume.
Another improvement of the moderator efficiency is the mixing of mesitylene with other methyl-benzene compounds. As shown in ch. 5.2 the more efficient amorphous phase II of mesitylene is metastable and difficile to obtain. Solutions of mesitylene with m-xylene or toluene crystallise in amorphous solids which are stable in the whole temperature range below the melting point [18].

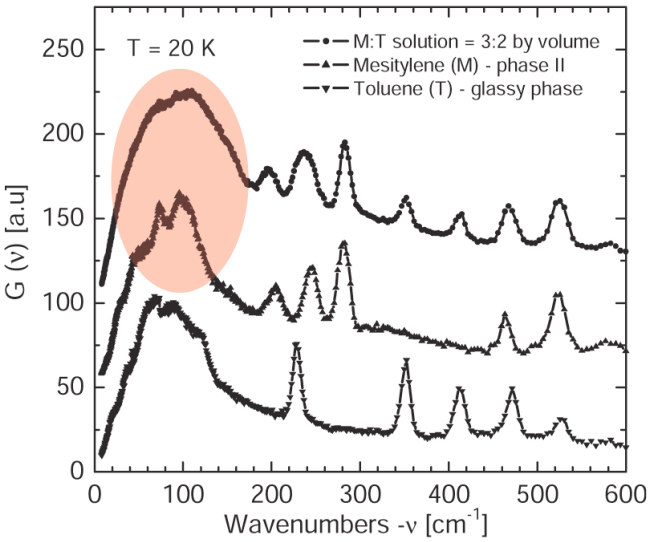

Figure 59: Vibrational spectra of a 3:2 mixture of mesitylene and toluene in comparison with phase II mesitylene at $T = 20\,\mathrm{K}$ [18].

Fig. 59 shows the vibrational spectra of a 3:2 mesitylene/toluene mixture measured at 20 K. The red marked area points out the significant higher amount of DOS in the low frequency regime of the mesitylene/toluene mixture compared to phase II mesitylene which qualifies the mixture to be a superior cold moderator material.
In combination with the previously presented concepts this is a promising approach to distinctly improve the moderation efficiency, handling and reliability of organic compound based cold moderator systems.

In this thesis a cryogenic moderator system based on mesithylene has been analysed. The comparison with literature has shown that the performance of a cryogenic moderator depends on the surrounding geometry. Possibilities for further investigations and improvements to enhance the performance of a mesitylene cold moderator system has been proposed. It has been shown that mesitylene is a reasonable moderator material for cryogenic temperatures at around 20 K which is easy to use but offers a good performance.

A Acknowledgment

At this point I would like to thank Prof. Dr. Thomas Brückel for the proposal of the interesting topic of this master thesis.

Prof. Dr. Oliver Pooth for examining the thesis as second assessor.

Thanks to Dr. Paul Zakalek for the helpful advices especially in python programming, a lot of patience and proofreading the thesis, to Annika Stellhorn, Dr. Johannes Baggemann and Marius Rimmler for proofreading and Dr. Günter Kemmerling for practical advices regarding ^3He detectors.

Many thanks also to all colleagues in the HBS team and the staff of the JCNS institute for the good teamwork.

B Declaration

This master thesis is my own independent work and is the result of my sole efforts. No other sources or references have been used in its production apart from the quoted ones.

Aachen, 14.9.2020 _____

Mathias Strothmann

References

[1] Thomas Brückel. *Neutron Scattering Lectures of the JCNS Laboratory Course held at Forschungszentrum Jülich and at the Heinz Maier-Leibnitz Zentrum Garching In cooperation with RWTH Aachen and University of Münster*. Forschungszentrum Jülich GmbH, Jülich, 2015.

[2] Markus Büscher. K+-Meson production in nucleii. Universität Köln. Habilitation, 2004.

[3] F. Cantargi, J.J. Blostein, L. Torres, and J.R. Granada. Thermal neutron cross section of liquid and solid mesitylene. *Nuclear Instruments and Methods in Physics Research Section B: Beam Interactions with Materials and Atoms*, 248(2):340–342, aug 2006.

[4] François Cardarelli. *Materials Handbook (Set/2 Bd))*. Springer-Verlag GmbH, 2018.

[5] T. Cronert, J. P. Dabruck, P.-E. Doege, Y. Bessler, M. Klaus, M. Hofmann, P. Zakalek, U. Rücker, C. Lange, M. Butzek, W. Hansen, R. Nabbi, and T. Brückel. High brilliant thermal and cold moderator for the HBS neutron source project Jülich. *Journal of Physics: Conference Series*, 746:012036, sep 2016.

[6] Jan Philipp Dabruck. *Target Station Optimization for the High-Brilliance Neutron Source HBS*. Springer-Verlag GmbH, 2018.

[7] Louis de Broglie. *Recherches sur la théorie des Quanta*. PhD thesis, Sorbonne university, Paris, 1925.

[8] Wolfgang Demtröder. *Experimentalphysik 1*. Springer Berlin Heidelberg, 2008.

[9] Ralf Engels. *Entwicklung eines Prototypen für einen großflächigen Szintillationsdetektor zur Detektion thermischer Neutronen*. PhD thesis, Universität Freiburg, 2011.

[10] D. Evans. Irradiation effects in liquid methane used as a neutron moderator. *Cryogenics*, 35(11):763–766, nov 1995.

[11] P. Doege J. Fenske M. Feygenson A. Glavic O. Holderer S. Jaksch M. Jentschel S. Kleefisch H. Kleines J. Li K. Lieutenant P. Mastinu E. Mauerhofer O. Meusel S. Pasini H. Podlech M. Rimmler U. Rücker T. Schrader W. Schweika M. Strobl E. Vezhlev J. Voigt P. Zakalek O. Zimmer J. Baggemann, S. Böhm. *Conceptual Design Report - Jülich High Brilliance Neutron Source (J-HBS)*. Forschungszentrum Jülich GmbH, 2020.

[12] E. Kulagin, S. Kulikov, V. Melikhov, and E. Shabalin. Radiation effects in cold moderator materials: Experimental study of accumulation and release of chemical energy. *Nuclear Instruments and Methods in Physics Research Section B: Beam Interactions with Materials and Atoms*, 215(1-2):181–186, jan 2004.

[13] ESFRI Physical Sciences and Engineering Strategy Working Group. *Neutron scattering facilities in Europe - Present status and future perspectives*, volume ESFRI Scripta Volume I. Dipartimento di Fisica - Università degli Studi di Milano, 2016.

[14] Forschungszentrum Jülich GmbH. Vorrichtung zur Erzeugung von thermischen Neutronenstrahlen mit hoher Brillianz und Herstellungsverfahren. EU-Patent - EP 3091 540 A1, 2016.

[15] Sigma-Aldrich Inc. Product catalog, 2020. `https://www.sigmaaldrich.com/catalog/product/sial/m7200?lang=de&region=DE`.

[16] Sigma-Aldrich Inc. Sicherheitsdatenblatt Mesitylen, 2020. version 6.1.

[17] The Nuclear Energy Agency (NEA). *JANIS database*, (accessed August 3,2020).

[18] I. Natkaniec, K. Holderna-Natkaniec, and J. Kalus. Neutron scattering studies of methyl derivatives of benzene selected as potential materials for cold neutron moderators. *Physica B: Condensed Matter*, 350(1-3):E651–E653, jul 2004.

[19] K. Nünighoff, Ch. Pohl, S. Koulikov, F. Cantargi, H. Conrad, D. Filges, H. Glückler, F. Goldenbaum, R. Granada, G. Hansen, T. Matzerath, N. Paul, S. Petriw, H. Schaal, H. Soltner, H. Stelzer, W. Ninaus, and M. Wohlmuther. Neutron experiments with cryogenic methane hydrate and mesitylene moderators. *The European Physical Journal A*, 38(1):115–123, oct 2008.

[20] Wolfgang Nolting. *Grundkurs Theoretische Physik 6.* Springer-Verlag GmbH, 2013.

[21] Kay Nünighoff. *Sicherheitstechnik im Wandel nuklearer Systeme Strahlenschutz bei Spallationsneutronenquellen und Transmutationsanlagen.* Forschungszentrum Jülich, Zentralbibliothek, Jülich, 2009.

[22] M. Huerta Parajon, E. Abad, and F.J. Bermejo. A Review of the Cold Neutron Moderator Materials: Neutronic Performance and Radiation Effects. *Physics Procedia*, 60:74–82, 2014.

[23] O. Felden R. Gebel, R. Brings and R. Maier. Operation of the injector cyclotron JULIC for the cooler synchrotron COSY/Jülich. *Proceedings of the 18th International Conference on Cyclotrons and Their Applications 2007, CYCLOTRONS 2007*, 01 2007.

[24] M. Rimmler, J. Baggemann, P-E Doege, Jiatong Li, Jing Li, E. Mauerhofer, O. Felden, N.-O. Fröhlich, R. Gebel, U. Rücker, M. Strothmann, Y. Valdau, P. Zakalek, T. Gutberlet, and T. Brückel. Determination of the neutron yield of Be, V and Ta targets irradiated with protons (22-42 MeV) by means of prompt gamma neutron activation analysis. *Nuclear Instruments and Methods in Physics Research Section A*, 2020 (to be published).

[25] N. K. Roy, D. Behera, O. G. Dibua, C. S. Foong, and M. A. Cullinan. A novel microscale selective laser sintering (μ-SLS) process for the fabrication of microelectronic parts. *Microsystems & Nanoengineering*, 5(1), dec 2019.

[26] U. Rücker, T. Cronert, J. Voigt, J. P. Dabruck, P. E. Döge, J. Ulrich, R. Nabbi, Y. Beßler, M. Butzek, M. Büscher, C. Lange, M. Klaus, T. Gutberlet, and T. Brückel. The jülich high-brilliance neutron source project. *The European Physical Journal Plus*, 131(1), jan 2016.

[27] Robin Jürgen Similon. Thermische Analyse der Wärmeflüsse eines Mesitylen-Neutronen-Moderator-Systems im kryogenen Temperaturbereich. Bachlor´s thesis. University of applied sciences Aachen, 2019.

[28] S. Tasaki, Y. Idobata, Y. Adachi, F. Funama, and Y. Abe. Study on Moderation Properties of Cold Mesitylene using KUANS. *EPJ Web of Conferences*, 231:04005, 2020.

[29] R. Dean Taylor and John E. Kilpatrick. Entropy, Heat Capacity, and Heats of Transistion of 1,3,5-Trimethylbenzene. *The Journal Of Chemical Physics*, 23(7), july 1955.

[30] K. Ünlü, C. Rios-Martinez, and B. W. Wehring. Prompt Gamma Activation Analysis with the Texas Cold Neutron Source. *Journal of Radioanalytical and Nuclear Chemistry Articles*, 193(1):145–154, may 1995.

List of Figures

List of Tables